Minimizing bubble losses in membraneless flow-through water electrolysis

Gilles Deiters

Delft University of Technology

TU Delft

Minimizing bubble losses in membraneless flow-through water electrolysis

by

Gilles Deiters

Student Name	Student Number
G. B. Deiters	4670612

Thesis supervisor:	Dr. Ir. J. W. Haverkort
Daily supervisor:	Ir. J. I. Postma
Thesis committee:	Dr. H.B. Eral
	Dr. A.J.L.L. Buchner
Project Duration:	November, 2022 - August, 2023
Faculty:	Process & Energy, Delft

TU Delft

Abstract

In an effort to make water electrolysis more efficient and simple, flow-through electrolyzers eliminate the need for a gas-separating membrane between the electrodes. However, replacing the membrane with a forced flow field brings new challenges and considerations. In this research, the design of a flow-through electrolyzer is optimized for minimum voltage losses due to bubble formation, pressure drop, and electrolytic resistance. These parameters are all influenced by the potassium hydroxide concentration, the inter-electrode gap and the feed flow rate. The effect on the power dissipation of a flow-through electrolyzer is analytically modelled and validated using experiments, where the design variables are varied.

Additionally, the effect on the resistance in the electrolyte of keeping the gasses dissolved in the electrolyte is studied using IV curves of degassed electrolyte. The gasses in the electrolyte were purged with a vacuum chamber. This degassed electrolyte showed a reduction in overpotential of 150 mV at max. However, this reduction in overpotential was outweighed by the energy requirements to degas the electrolyte. Besides degassing, the effect of suppressing bubble formation by different flow rates was investigated. It was found that there was no noticeable reduction in overpotential between the state where bubbles are suppressed and bubbles were formed.

In addition to the effect of keeping the gasses dissolved, an analytical model was constructed to describe the necessary flow rates to mitigate the electrical resistance due to bubbles in the electrolyte. In the analytical model, solubility plays a big role in determining the necessary flow rate, as solubility is related to the emergence of bubbles. Contrarily, experiments showed the effect of solubility was found to be rather low. By varying the gap width, it was shown that the shear rate at the wall is a better indicator for bubble removal and therefore reduction in resistance due to bubbles.

Furthermore, the shape of the discharge channel was changed to promote uniform flow across the electrodes. The uniform flow should make the product removal at every part of the electrolyzer equal, such that there are no stagnant zones where gas accumulation could build up. This new discharge channel shape was analysed using COMSOL Multiphysics by comparing it with a conventional straight discharge channel. The variable discharge channel outperformed the straight discharge channel in creating a uniform flow across the electrodes for Euler numbers bigger than 10, meaning that the inertial forces are negligible compared to the pressure drop. During experiments, the electrolyzer with a variable discharge channel was tested. This electrolyzer configuration did not perform as well as expected from the theory and simulations, having a higher pressure drop and electric resistance than the conventional electrolyzer. The reason why the variable discharge channel performed poorly was inconclusive.

Lastly, the performance of the various variables was evaluated using the total power dissipation as a function of the current density. This took both the pressure drop across the system and the electrical power consumption of the electrolyzer into account. It was found that using a high electrolyte of 6M potassium hydroxide (KOH) together with a small inter-electrode gap gave the lowest energy dissipation per kg produced hydrogen gas. However, increasing the KOH concentration increases the viscosity and thereby the pressure drop. The theoretical optimum for KOH concentration was calculated to be 5M for this flow-through electrolyzer

Acknowledgements

Doing a master's thesis was a tremendously fun experience. It was hard work, but rewarding. Even though you supposedly need to do the master's thesis on your own, I could not have done it alone. I was very lucky to find my great supervisor Willem Haverkort and his PhD candidate Jelmer Postma. They were quick to reply and kept sparking my curiosity about the subject. Our critical discussions helped me better understand electrolyzers and how to improve them. Together with them, we made most of the analytical relations shown in the theory section of this thesis. I also want to thank the PhD students at Willem's research group for their well-established feedback on my presentations and theories. I want to give my gratitude to all the other master's students for joining in our complaining about the limited space available. I want to thank the people at the Mexican food truck for making delicious quesadillas every Thursday at 12:00 after our group meeting.

I want to give a special thanks to Emile Craye, who helped me make the nice cover foto for my master's thesis. I also want to thank Caiwei Zhu for checking my thesis's grammar, for her moral support and

listening to my constant rambling about hydrogen. I want to express my gratitude to my parents for making delicious food and sponsoring my mechanical engineering studies. I want to thank my rowing crew and coaches for giving me space in stressful times.

It was a long journey up the mountain of weird projects, painful assignments and dubious working hours, but it was fun and I would do it again if I had the choice.

"Je gaat het pas zien als je het door hebt."
Johan Cruijff, 1994

Contents

Nomenclature

Symbols

Constant	Description	Value	Unit
Physics constants			
F	Faraday constant	96485	C mol^{-1}
M_{H_2}	Molecular weight of hydrogen	2.016	g mol^{-1}
Z	Number of electrons per reactant molecule in water electrolysis at the hydrogen side (cathode)	2	[-]
Fluid variables			
c_{KOH}	Potassium hydroxide concentration		M
Eu	Euler number		[-]
$\dot{\gamma}$	Wall shear rate		s^{-1}
k	Permeability		m^2
κ	Ionic conductivity		S m^{-1}
μ	Dynamic viscosity		Pa s
p	Pressure		Pa
Q	Volumetric flow rate		m^3 s^{-1}
Q_{min}	Experimental required minimum volumetric flow rate		m^3 s^{-1}
Q_{th}	Theoretical required minimum volumetric flow rate		m^3 s^{-1}
Re	Reynolds number		[-]
ρ	Mass density		kg m^{-3}
ρ_{H_2}	Specific density of hydrogen gas		mol m^{-3}
S	Solubility		[mol H_2] [L H_2O]$^{-1}$
S_V	Volumetric solubility		[mL H_2] [L H_2O]$^{-1}$
T	Temperature		K
u	The real velocity across the electrode		m s^{-1}
U	Superficial velocity across the electrodes		m s^{-1}
$\overline{U}(z)$	Normalized superficial velocity across the electrodes		[-]
U_i	Ideal superficial velocity across the electrodes		m s^{-1}
$U_m(z)$	Modelled superficial velocity across the electrodes		m s^{-1}
U_{th}	Theoretical required minimum volumetric flow velocity		m^3 s^{-1}
$w_d(z)$	Vertical velocity in the discharge channel		m s^{-1}
$w_f(z)$	Vertical velocity in the feed channel		m s^{-1}
Geometric dimensions			
A	Electrode Area		m^2
D	Electrode hole diameter		m
H	Height of the electrodes		m
$l_d(z)$	Discharge channel width		m
l_e	Electrode width		m
l_f	Inter electrode gap / Feed channel width		m
l_y	Width of the electrode in the y-direction		m
n	number of holes in the electrode		[-]
x	x-coordinate		m

y	y-coordinate		m
z	z-coordinate		m
$\hat{z}_{\text{co}}$	Cut-off height		[-]
Electrical variables			
η_0	Efficiency calculated with the equilibrium potential		[-]
η_T	Efficiency calculated with the thermal neutral voltage		[-]
j	Current density		A m^{-2}
ϕ_0	Equilibrium potential for water electrolysis	1.48	V
ϕ_{a}	Activation overpotential		V
ϕ_{an}	Anodic reaction potential for alkaline water electrolysis	0.83	V
ϕ_{cell}	Cell potential		V
ϕ_{cth}	Cathodic reaction potential for alkaline water electrolysis	0.83	V
ϕ_T	Thermoneutral voltage	1.48	V
$\Delta\phi_{\text{vac}}$	Overpotential reduction by vacuum degassing the electrolyte		V P_Ω
Ohmic power dissipation		W	
R_Ω	Ohmic resistance		Ω
Other			
C	Constant		[-]
E_{H_2}	Energy consumption per produced kg hydrogen		J/kg
E_{HHV}	Higher heating value of hydrogen	142	MJ/kg
$\dot{n}$	Molar flow rate		mol s^{-1}
p_{atm}	Atmospheric pressure	1	bar
P_{pres}	Pressure power dissipation		W
P_{tot}	Total power dissipation		W

1 Introduction

Hydrogen is a reliable and environmentally friendly energy carrier [1]. It can be used in fuel cells to produce electricity and as an alternative fuel for the transportation industry. Another promising application is to reduce emissions in industries like the steel industry [2], or the chemical industry [3], where hydrogen is often used as a raw material. One significant advantage of using hydrogen is that it does not emit any greenhouse gasses during combustion. Currently, there are two common ways of obtaining hydrogen, as a product of the fossil industry or by using water electrolysis to split water into hydrogen and oxygen. The former requires the gasification of fossil resources, which produces greenhouse gasses. The latter is carbon emission-free. Furthermore, using water electrolysis can be directly coupled with renewable energy sources such as wind and solar. However, hydrogen is still produced mainly as a product of the fossil industry. Only 4% of the global hydrogen production in 2021 is using water electrolysis [4]. This is because it has a lower production cost than water electrolysis [5]. Obtaining hydrogen using water electrolysis is bound to the electricity price. Increasing the efficiency of an electrolyzer is therefore of great interest to lower the production cost of hydrogen using water electrolysis. The current two main water electrolyzer types are the proton-exchange membrane (PEM) electrolyzer and the alkaline water electrolyzer (AWE). There are advantages and disadvantages to using one over the other [6]. PEM can run at current densities at a certain voltage higher than those of AWE. This effectively means that a PEM has more hydrogen production per electrode area than an AWE at the same efficiency. AWE on the other hand is cheaper and more durable. This makes it a viable option because, as mentioned before, one of the biggest limitations of water electrolysis is the cost. Besides this, there is still room to improve the alkaline water electrolyzer. One example is removing the gas-separating membrane in an AWE, which improves the efficiency of the system and makes the electrolyzer more durable and less complex.

1.1. Membraneless alkaline water electrolysis

Between the electrodes of a conventional AWE, there is a membrane that prevents hydrogen and oxygen from mixing into an explosive mixture. This membrane increases the complexity of the system and reduces its efficiency. For this reason, the removal of the membrane reduces the capital and operational cost of the AWE [7]. Furthermore, removing the membrane allows the inter-electrode gap to decrease, which removes the necessity for highly concentrated electrolytes. Without a membrane, the challenge is to find an alternative way to separate hydrogen and oxygen gas. A possible solution is to use an induced flow to prevent hydrogen and oxygen from mixing. Because hydrogen is made at the cathode and oxygen is made at the anode, the flow can direct these gasses away from each other. This method of separating the gasses in an electrolyzer is called the membraneless flow electrolyzer. Membraneless flow electrolyzers come in two main categories: The flow-by electrolyzer and the flow-through electrolyzer. There are many more types of membraneless electrolyzers, such as buoyancy-driven, concentration-driven, capillary-driven or using decoupled reactions [8], but this is beyond the scope of this research because they do not rely on forced convection. The flow-by configuration is presented on the left and the flow-through is shown on the right Fig. 1.1. The exact working principles of these two electrolyzers will be explained in their own sections.

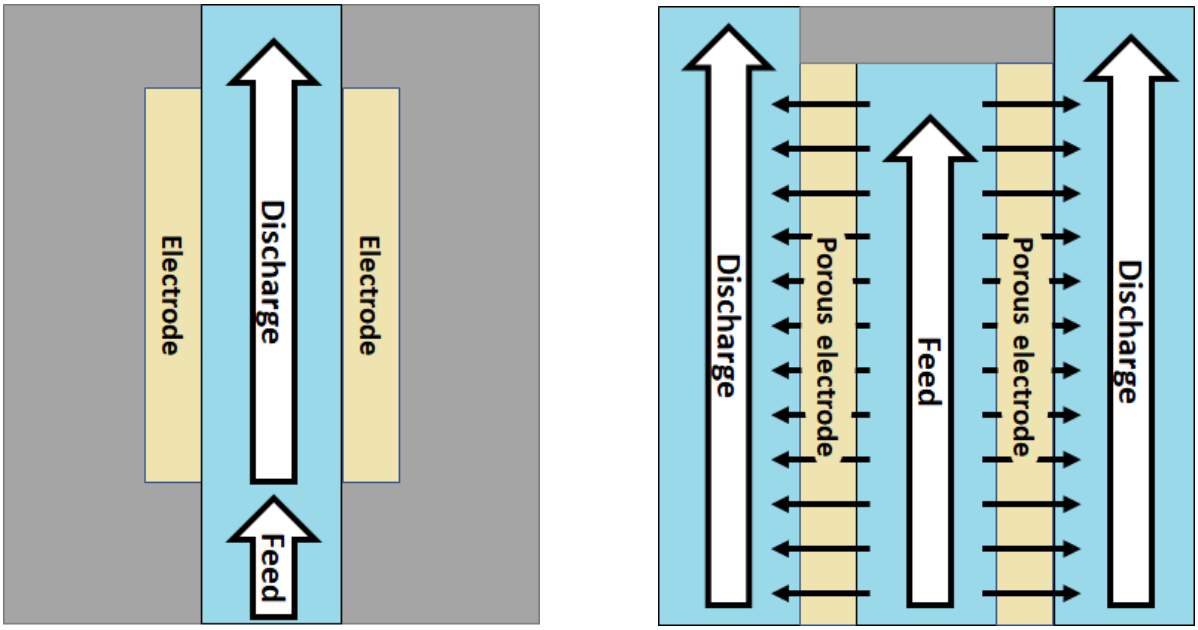

Figure 1.1: A representation of the flow in a flow-by electrolyzer (left) and a flow-through electrolyzer (right)

1.2. Flow-by electrolyzer

In the flow-by configuration, the electrolyte flows parallel between the two electrodes. When flowing fast enough, the Péclet number is high, which means low diffusion compared to advection, which prevents gas crossover [9]. Another possibility is to make use of the Segré-Silberberg effect [10] on bubbles to prevent gas-crossover [11–15]. However, as Pang et al. [14] concluded, it is not yet possible to achieve high current densities and efficiencies without hydrogen and oxygen crossover. This is because, at higher current densities, a high flow is needed to ensure product removal. The problem is that at higher flows the Reynolds number becomes large, and the flow becomes turbulent, which potentially causes the mixing of the gasses.

1.3. Flow-through electrolyzer

In a flow-through electrolyzer, the flow is directed through the electrodes, as shown in Figure 1.1. This way, the separation is governed by pushing the two products away from each other. The flow-through electrolyzer with membranes has already been researched for decades [16–20]. Recently, Gillespie et al. [21] sparked new interest in this type of electrolysis in 2015, when they made a flow-through electrolyzer without the use of a gas-separating membrane. In a later study, they created a device, called the ”DEFT” [22] that was able to produce hydrogen at a current density of 4 A/cm^2 at an efficiency of 35%. O'Neal et al. [23] investigated the effect of the angle between the two electrodes. With their flow-through electrolyzer, they managed to generate hydrogen at 0.1 A/cm^2 at a 72% efficiency. Both flow-through setups show considerably better performance than the flow-by configuration. This can be seen in the work of Manzotti et al. [8], where they summarized the performance of the flow-through electrolyzer compared to the flow-by electrolyzer, showing the improved efficiency of the flow-through electrolyzer over the flow-by electrolyzer. The efficiency of the flow-through electrolyzer can still be improved as shown in the study by Rajaei et al. [24], where they investigated the optimal design parameters, such as the effect of the inlet velocity and optimal inter-electrode gap to further reduce losses in the device. In this report, the goal is to further optimize the efficiency of the flow-through electrolyzer by negating losses due to bubble formation and investigating the effect of keeping hydrogen and oxygen saturated in the liquid. This means that no bubbles are produced, negating losses due to poor current distribution [25], the surface coverage of the electrodes, and increased electrolytic resistance [26]. To keep the gasses saturated in the liquid, it is important that the flow passes every part of the electrodes evenly. This avoids build-up of gasses at certain spots on the electrode and creates bubbles which would create additional losses. To do this, the shape of the discharge channel is adjusted to improve the uniformity of the flow across the electrodes, which can be seen in Fig. 2.2.

This new discharge channel design will be evaluated with a numerical study in COMSOL Multiphysics and by means of lab experiments.

1.4. Research scope

To conduct the research in a structured manner, the following research question is introduced:

What geometry and fluid variables achieve the lowest power dissipation at atmospheric conditions in an alkaline flow-through water electrolyzer in order to minimize the losses due to bubble formation?

Following with the subquestions to help answer the main research question:

- What effect on efficiency does keeping hydrogen and oxygen gas dissolved in the electrolyte have on a flow-through alkaline water electrolyzer?
- What flow rate is needed to keep the energy losses in an electrolyzer due to bubble formation and pressure drop at a minimum?
- What shape does the discharge channel need to be to distribute the flow uniformly across the electrodes, to ensure saturation across the electrode of product gasses and to keep the pressure drop across the electrodes at a minimum?
- What is the optimal potassium hydroxide concentration for running the electrolyzer?

In this research, the setup will be kept at room temperature (25 °C) and atmospheric pressure for simplicity. The efficiency can be greatly improved with higher temperatures, increasing ionic conductivity [27], and pressures, increasing gas solubility [28], and will therefore be added as a recommendation for future research.

Furthermore, in the experiments, the gas cross-over will not be measured. This is necessary to be done in future research because the mixing of hydrogen and oxygen can cause explosion hazards [29] and because it is desirable to produce hydrogen at purities above 99.9 % for fuel cell applications following ISO 14687-3 (Type I Grade E).

The electrolyte is an alkaline solution of potassium hydroxide (KOH). KOH is usually used in water electrolysis. This is because it allows the use of electrode materials which are cheaper and less susceptible to corrosion than the materials used in acidic solutions [30]. Another option instead of KOH would be sodium hydroxide (NaOH), but the former has a higher ionic conductivity [31] and is, therefore, a better option for a high-efficiency electrolyzer.

2 Theory

An alkaline water electrolyzer consists of two electrodes which are submerged in water. The ionic conductivity of water is increased using an alkaline electrolyte, in this case, KOH. When an electrical current is established between the two electrodes, the water starts to split into hydrogen and oxygen gas in a reaction spanning over the two electrodes. At the negatively charged electrode, the cathode, water reacts to hydrogen gas and hydroxide ions. At the positively charged electrode, the anode, the hydroxide ions react to oxygen and water. These two half-reactions are specific to alkaline solutions and are presented with their reduction potential below:

$$\begin{aligned} \text{Cathode:} \quad & 2H_2O + 2e^- \rightarrow 2H_2 + 2OH^- && \phi_c = \text{-0.40 V} \\ \text{Anode:} \quad & 2OH^- \rightarrow \tfrac{1}{2}\, O_2 + 2H_2O + 2e^- && \phi_a = 0.83 \text{ V} \end{aligned}$$

2.1. Electrolysis losses

During operation, the electrolyzer experiences losses in addition to the theoretical energy required to split hydrogen and oxygen. These losses can be decoupled into two parts, the activation overpotential and the ohmic overpotential. In water electrolysis, the performance is often measured in current densities vs voltage, this is because current density is proportional to the amount of hydrogen produced per unit area. High production of hydrogen per electrode area means that the capital cost is low for a certain production capacity. Current is then a product of the current density and the electrode area,

$$I = jA \tag{2.1}$$

Current density is used in this chapter and throughout the report as a measure of performance.

2.1.1. Equilibrium potential

In theory, the electrolysis reaction starts to occur when the equilibrium potential is applied. The equilibrium potential is the sum of two half reaction potentials, $\phi_0 = \phi_{\text{cth}} + \phi_{\text{an}} = -1.23$ V. This equilibrium potential is often used as a measure of efficiency,

$$\eta_0 = \frac{1.23 \text{ V}}{\phi_{\text{cell}}} \tag{2.2}$$

With ϕ_{cell} the cell voltage. In reality, there is additional energy required to maintain a thermal balance. If this additional energy is taken into account, the voltage needed to sustain the reaction is $\phi_T = 1.48$ V. The efficiency can then be calculated using the thermoneutral voltage,

$$\eta_T = \frac{1.48 \text{ V}}{\phi_{\text{cell}}} \tag{2.3}$$

2.1.2. Activation overpotential

In addition to the equilibrium potential, there is an activation overpotential which is caused by the activation energy of the cell [32]. This activation overpotential is logarithmically dependent on the applied current density of the cell. The activation overpotential is also dependent on material and surface geometry. Materials like copper and iron have low activation overpotentials but are not resistive to an alkali environment. The next best option is nickel due to its chemical resistivity and low capital cost [33]. In general, the activation overpotential can be expressed in the following form:

$$\phi_{\mathsf{a}} = b \ln(j) \tag{2.4}$$

b is the Tafel slope, which is dependent on temperature and the material properties of the electrodes. Because in this research, the temperature and material properties are not investigated, a is assumed constant.

2.1.3. Ohmic overpotential

The ohmic overpotential is caused by the losses in the electrolyte. In general, the losses can be described by Pouillet's law:

$$R_\Omega = \frac{l}{\kappa A} \tag{2.5}$$

The Ohmic overpotential can be expressed as the following:

$$\phi_\Omega = jAR_\Omega = \frac{jl}{\kappa} \tag{2.6}$$

To minimize the losses, the inter-electrode distance, l, can be decreased or the ionic conductance, κ, can be increased, for example by the use of a more potent electrolyte. A membrane has a lower effective conductivity and increases the resistance in the electrolyte. This resistance is removed by using a Flow-Through electrolyzer without a membrane. Additionally, Bubbles create extra resistance in the electrolyte, because they block the path of ion flow. For this research, the losses due to bubbles are particularly interesting and they are tried to suppress.

Combining the potentials together forms an IV curve, which can be used as a means to measure the performance of an electrolyzer for various current densities.

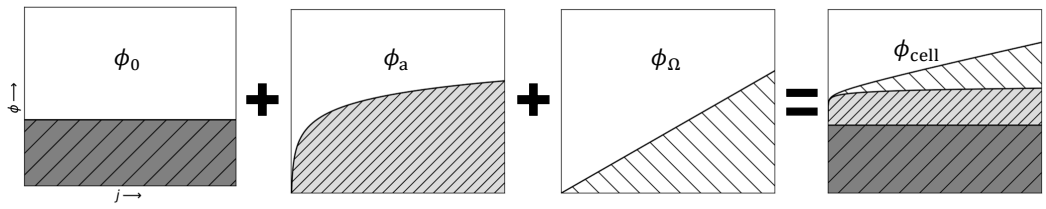

Figure 2.1: Representation of the contributions to cell potential. From left to right: Thermoneutral overpotential, activation overpotential, ohmic overpotential and the cellpotential

2.2. Shape of the discharge channel

The flow geometry is introduced in Fig. 2.2, where important geometric parameters used in the equations in this chapter are shown.

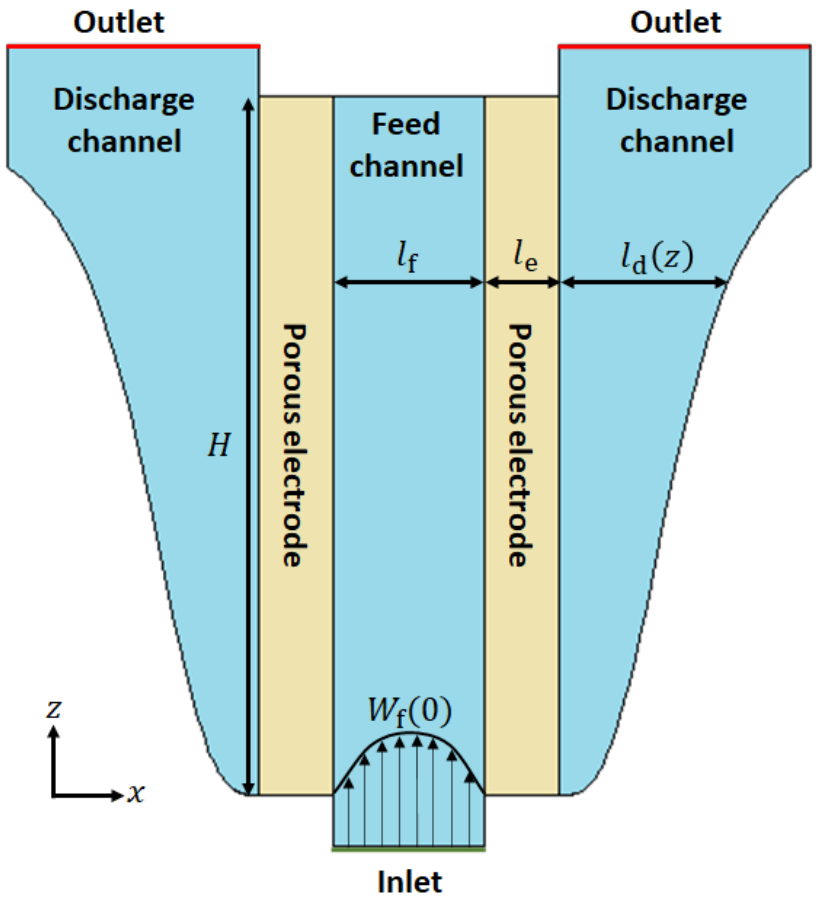

Figure 2.2: 2D geometry of the design with the important geometrical dimensions given

The feed channel in the middle and the discharge channels at the sides are separated by porous electrodes. The discharge channel has a shape formed by the function, l_d. The shape will be analytically calculated in section 2.2. In section 2.4 the required inlet velocity is calculated to be sure that the gasses stay saturated. Section 2.5 will show the optimum inter-electrode gap, l_f, to create the least power dissipation during operation.

During electrolysis, the production of hydrogen is uniform across the porous electrodes assuming a uniform current distribution. To negate the losses due to bubbles, hydrogen, and oxygen are removed from the electrode using forced convection. To be sure that there are no areas with limited dissolved gas removal, the flow has to be uniform across the electrode height. If the hydraulic resistance for each possible flow path from the inlet to the outlet is equal, the flow will distribute itself uniformly across the electrode. This means that the pressure drop across the electrodes needs to be the same. For this to happen, the gradient in the discharge channel and the feed channel need to match

$$\left[\frac{dp}{dz}\right]_d = \left[\frac{dp}{dz}\right]_f \tag{2.7}$$

Assuming Hagen-Poiseuille in both channels, the pressure gradient can be written in the form:

$$\frac{dp}{dz} = 12\mu\frac{W}{l^2} \tag{2.8}$$

Inserting Eq. (2.7) into Eq. (2.8), gives:

$$\frac{w_f}{l_f^2} = \frac{w_d}{l_d^2} \tag{2.9}$$

When the flow passes the electrodes uniformly, the feed velocity, w_f, will decrease linearly from bottom

to top:

$$w_{\mathsf{f}}(z) = w_{\mathsf{f}}(0)\left(1 - \frac{z}{H}\right) \tag{2.10}$$

Due to mass conservation, the relation between the feed velocity and the discharge velocity is:

$$w_{\mathsf{d}} l_{\mathsf{d}} = \frac{l_{\mathsf{f}}}{2}(w_{\mathsf{f}}(0) - w_{\mathsf{f}}(z)) \tag{2.11}$$

Substituting $w_{\mathsf{f}}(z)$ from Eq. (2.10) into Eq. (2.11), the following equation is obtained:

$$w_{\mathsf{d}}(z) = w_{\mathsf{f}}(0)\frac{z}{H}\frac{l_{\mathsf{f}}}{2l_{\mathsf{d}}} \tag{2.12}$$

Inserting equations (2.10) and (2.12), yields

$$\frac{w_{\mathsf{f}}(0)}{l_{\mathsf{f}}^2}\left(1 - \frac{z}{H}\right) = w_{\mathsf{f}}(0)\frac{z}{H}\frac{l_{\mathsf{f}}}{2l_{\mathsf{d}}^3} \tag{2.13}$$

When the width of the channels remains constant, Eq. (2.13) does not hold, meaning the flow will unevenly distribute across the electrodes. To solve this, it is possible to create a high-pressure drop across the electrodes, such that the imbalance in pressure gradients in the channels is negligible. A high-pressure drop can be achieved by, for instance, lowering the permeability of the electrodes. However, this requires additional pumping power in the system, decreasing the overall efficiency, and is, therefore, an undesirable approach. The other option is to allow the discharge channel and feed channel to change in width. Making the feed channel width variable in height interferes with the current distribution between the electrodes. Instead, the discharge channel is made variable in the z-direction. This does not change the inter-electrode gap, thus it does not change the current distribution. With Equation (2.13), the discharge channel width can be written as:

$$l_{\mathsf{d}}(z) = l_{\mathsf{f}}\sqrt[3]{\frac{\frac{z}{H}}{2\left(1 - \frac{z}{H}\right)}} \tag{2.14}$$

Figure 2.3 gives a representation of Eq. (2.14).

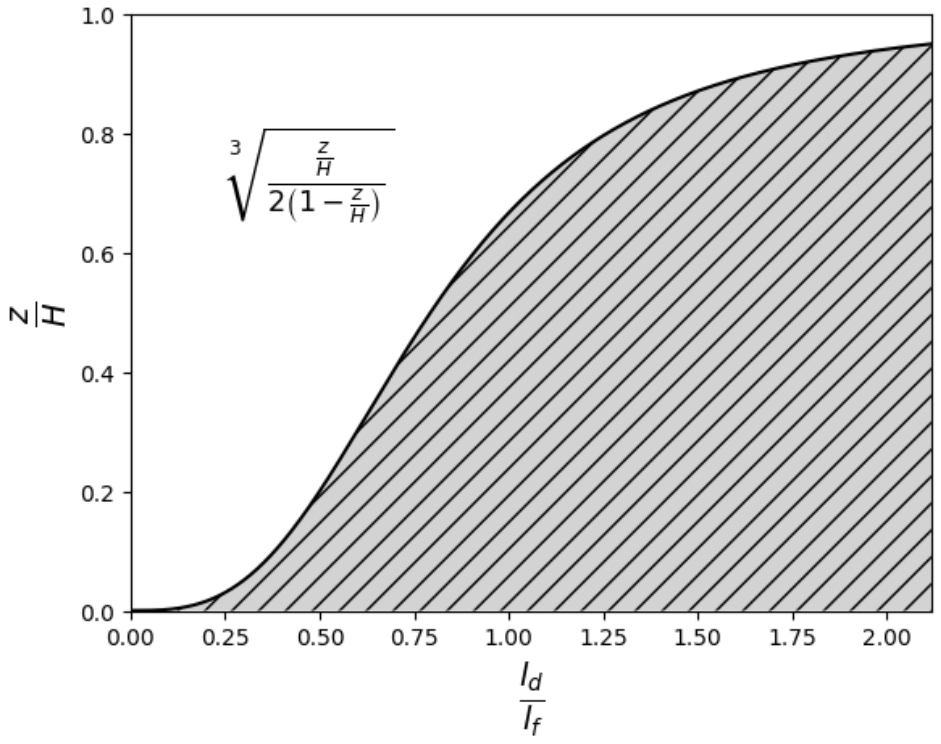

Figure 2.3: The geometry of the discharge channel in the xz-plane. The hatched area indicates the wall, and the white area is the fluid domain

2.3. Cutoff height

In equation (2.14), the width of the discharge channel goes to infinity at $z = H$. This is because the feed channel velocity and, thus, the pressure drop reaches zero at the top of the channel requiring the discharge channel to be infinitely wide to match this zero pressure drop. This is not possible in reality, therefore the top of the geometry needs to be cut off and made vertical. The relative height where the geometry is cut off is called the cut-off height, $\hat{z}_{\text{co}}$. For example, $\hat{z}_{\text{co}} = 0.8$ means that the top 20% of the geometry height will be cut off and made vertical. This is illustrated in figure 2.4

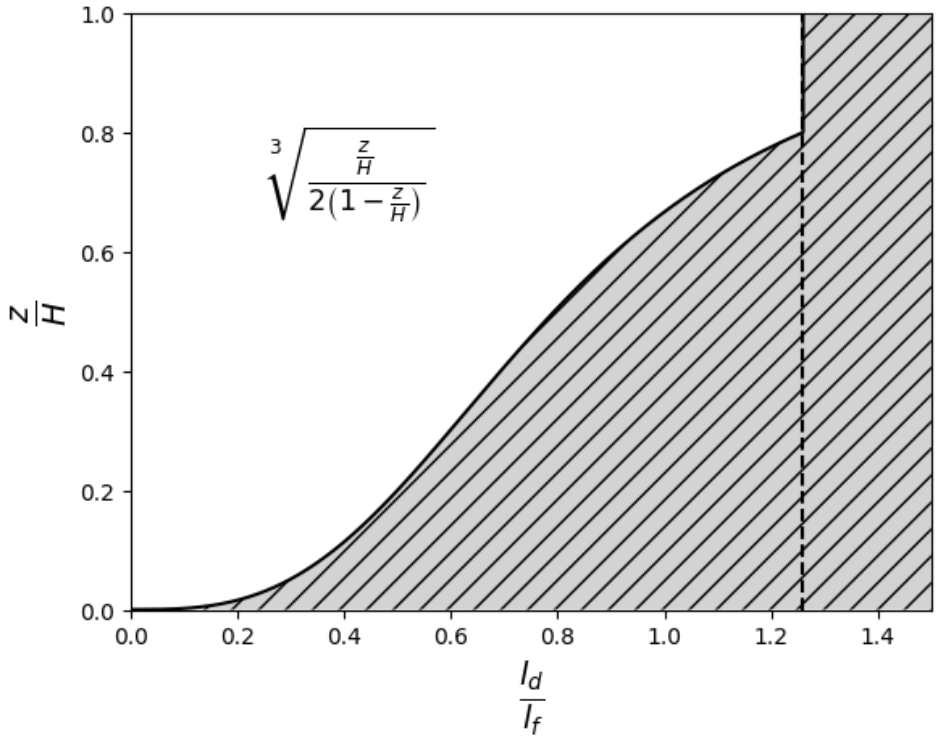

Figure 2.4: In this figure, the flow geometry is cut off at $\hat{z}_{\text{co}} = 0.8$, which is indicated by the dashed line

2.4. Mass transport

In the cell, a forced flow is driven by a pump to transport the hydrogen and oxygen through the electrodes. In the design, the flow velocity needs to be high enough, such that hydrogen and oxygen stay saturated in the electrolyte. The flow is assumed to be uniform and constant throughout the whole electrode. The velocity of the flow is chosen such that the concentration stays below the hydrogen saturation in water, S in mol/m^3. Oxygen has a much higher solubility than hydrogen, therefore oxygen is assumed to be solved when the flow velocity to keep the hydrogen solved is met. First, the rate of hydrogen production is calculated using Faraday's law:

$$\dot{n} = \frac{I}{FZ} \tag{2.15}$$

Z is the number of mols electrons required in the reaction. If the concentration reaches saturation, an amount of $\dot{n} = QS$ moles is displaced every second per electrode. Using this equation together with equation (2.15), the following relation for volume flux is obtained:

$$Q_{\text{th}} = \frac{I}{FZS} \rightarrow U_{\text{th}} = \frac{j}{FZS} \tag{2.16}$$

The second equation is equation (2.16) means that the velocity over the electrode, U, has to be higher than U_{th} to be sure no bubbles are formed. It may be possible that hydrogen is supersaturated in the electrolyte to several times the solubility of hydrogen [34, 35]. The required inlet velocity to the feed

channel for 2 electrodes, due to mass conservation, is:

$$w_{\mathsf{f}}(0) = 2U_{\mathsf{th}}\frac{H}{l_{\mathsf{f}}} = 2\frac{jH}{FZSl_{\mathsf{f}}} \tag{2.17}$$

2.5. Power dissipation and optimum gap

The pressure drop and ohmic resistance in the cell are essential quantities to calculate the optimum feed channel width. The ohmic drop can be reduced by placing the anode and cathode closer together. At the same time, decreasing this gap increases the pressure drop according to Hagen-Poiseuille. In the next section, the optimum gap is explained as an optimum between these two phenomena given the lowest overall power dissipation.

2.5.1. Pressure drop

The pressure drop in a channel with a laminar flow can be calculated using Hagen-Poiseuille. The cell is designed such that every path through the system from the inlet to the outlet has the same hydraulic resistance, as calculated in Sec. 2.2. For this calculation, the path through the full length of the feed channel and through the very top of the electrode is taken. The pressure drop consists of two parts in series: The pressure drop in the feed channel and the pressure drop through the electrode:

$$\Delta p_{\mathsf{tot}} = \Delta p_{\mathsf{e}} + \Delta p_{\mathsf{f}} \tag{2.18}$$

Feed channel pressure drop The feed channel pressure drop is calculated using Hagen-Poiseuille:

$$\left[\frac{dp}{dz}\right]_{\mathsf{f}} = 12\mu\frac{w_{\mathsf{f}}}{l_{\mathsf{f}}^2} \tag{2.19}$$

The feed velocity linearly decreases from bottom to top:

$$w_{\mathsf{f}}(z) = w_{\mathsf{f}}(0)\left(1-\frac{z}{H}\right) = 2\frac{jH}{FZSl_{\mathsf{f}}}\left(1-\frac{z}{H}\right) \tag{2.20}$$

By substituting equation (2.20) into equation (2.19) and integrating z over the channel height, H, the pressure drop in the feed channel is obtained:

$$\Delta p_{\mathsf{f}} = 12\mu\frac{j}{FZS}\frac{H^2}{l_{\mathsf{f}}^3} \tag{2.21}$$

Electrode pressure drop For a porous electrode, Darcy's law can be used to calculate the pressure drop:

$$\left[\frac{dp}{dx}\right]_{\mathsf{f}} = \frac{\mu U}{k} \tag{2.22}$$

k is the permeability of the electrode. Assuming the velocity through the electrode to be independent of x, the pressure gradient can be integrated to get the pressure drop over the electrode:

$$\Delta p_{\mathsf{e}} = \frac{l_{\mathsf{e}}\mu U}{k} \tag{2.23}$$

The relation for velocity over the electrode in terms of the inlet velocity is achieved by rewriting Eq. (2.17) and inserting it in Eq. (2.23):

$$\Delta p_{\mathsf{e}} = \frac{l_{\mathsf{e}}\mu w_{\mathsf{f}}(0) l_{\mathsf{f}}}{2Hk} = \frac{\mu l_{\mathsf{e}}}{k}\frac{j}{FZS} \tag{2.24}$$

2.5.2. Pressure drop power dissipation

Adding Eq. (2.21) and Eq. (2.24), the total pressure drop is obtained:

$$\Delta p_{\mathsf{tot}} = 12\mu\frac{j}{FZS}\frac{H^2}{l_{\mathsf{f}}^3} + \frac{\mu l_{\mathsf{e}}}{k}\frac{j}{FZS} \tag{2.25}$$

The power dissipation due to a pressure drop is calculated using the following equation:

$$P_{\text{pres}} = Q\Delta p \tag{2.26}$$

Substituting $2Q_{\text{th}}$ from Eq. (2.16) and Eq. (2.25) into Eq. (2.26), Eq. (2.27) is obtained:

$$P_{\text{pres}} = 24\mu \left(\frac{j}{FZS}\right)^2 \frac{H^3 l_y}{l_{\text{f}}^3} + 2\frac{H l_{\text{e}} \mu l_y}{k} \left(\frac{j}{FZS}\right)^2 \tag{2.27}$$

2.5.3. Ohmic power dissipation

The ohmic dissipation is caused by the ohmic resistance in the electrolyte can be calculated using Pouillet's law,

$$R_\Omega = \frac{l_{\text{f}}}{\kappa l_y H} \tag{2.28}$$

From Ohm's law, assuming a constant current across the electrodes, the power dissipation is given by the following relation:

$$P_\Omega = I^2 R_\Omega = \frac{j^2 l_y H l_{\text{f}}}{\kappa} \tag{2.29}$$

2.5.4. Total power dissipation and optimal gap

By combining the pressure and ohmic power dissipation, from Eq. (2.27) and Eq. (2.29) respectively, the equation for total power dissipation is obtained:

$$P_{\text{tot}} = 24\mu \left(\frac{j}{FZS}\right)^2 \frac{H^3 l_y}{l_{\text{f}}^3} + 2\frac{H l_{\text{e}} \mu l_y}{k} \left(\frac{j}{FZS}\right)^2 + \frac{j^2 l_y H l_{\text{f}}}{\kappa} \tag{2.30}$$

It is now possible to determine for which feed channel gap, l_{f}, the power is minimal, thus obtaining the highest cell efficiency. Because j does not depend on l_{f}, which can be seen in Eq. (2.16), and the rest of the variables are either geometrical variables independent of l_{f} or physical constants, the second term in Eq. (2.30) can be removed. The value for the gap with the lowest power dissipation is obtained by finding the local minimum of Eq. (2.30):

$$\frac{d}{dl_{\text{f}}} P_{\text{tot}} = -72\mu \left(\frac{j}{FZS}\right)^2 \frac{H^3 l_y}{l_{\text{f}}^4} + \frac{j^2 l_y H}{\kappa} = 0 \tag{2.31}$$

Solving for l_{f}, the optimal electrode gap is found, equal to the findings of Ref. [24]:

$$l_{\text{f}} = \sqrt{\frac{H}{FZS}} \sqrt[4]{72\kappa\mu} \tag{2.32}$$

If Eq. (2.32) is inserted back into Eq. (2.30), the following is obtained:

$$P_{\text{tot}} = \underbrace{j^2 l_y \sqrt{\frac{H^3}{FZ}} \sqrt[4]{\frac{\mu}{S^2\kappa^3}} \sqrt[4]{72}}_{\text{Electrical}} + \underbrace{j^2 l_y \sqrt{\frac{H^3}{FZ}} \sqrt[4]{\frac{\mu}{S^2\kappa^3}} \sqrt[4]{\frac{8}{9}} + 2\frac{H l_{\text{e}} \mu l_y}{k} \left(\frac{j}{FZS}\right)^2}_{\text{Pressure}} \tag{2.33}$$

When the permeability is high enough to neglect the last term of the equation, this leads to:

$$P_{\text{tot}} = j^2 l_y \sqrt{\frac{H^3}{FZ}} \sqrt[4]{\frac{\mu}{S^2\kappa^3}} \left[\underbrace{\sqrt[4]{72}}_{\text{Electrical}} + \underbrace{\sqrt[4]{\frac{8}{9}}}_{\text{Pressure}} \right] = \underbrace{C}_{\text{Electrical}} + \underbrace{\frac{1}{3}C}_{\text{Pressure}} \tag{2.34}$$

With $C = j^2 l_y \sqrt{\frac{H^3}{FZ}} \sqrt[4]{\frac{\mu}{S^2\kappa^3}} \sqrt[4]{72}$, which is the contribution of electrical losses to the total power dissipation. This means that 1/4 of the power dissipation is due to the pressure drop in the feed channel if the permeability is high enough to neglect the pressure drop across the electrodes.

2.5.5. Optimal potassium hydroxide concentration

The fluid variables viscosity, [36], ionic conductivity [27] and solubility [37] are all dependent on temperature and potassium hydroxide concentration. The dependency on the concentration of these variables is documented in Appendix A. This means that the power dissipation is also dependent on these two variables. For simplicity, the effect of temperature will not be investigated and the temperature is assumed to be 25 °C. The optimal KOH concentration can be found using Eq. (2.30). Inserting the optimal gap from Eq. (2.32) into Eq. (2.30), yields

$$P_{\text{tot}} = j^2 l_y \sqrt{\frac{H^3}{FZ}} \left[\sqrt[4]{\frac{\mu}{S^2\kappa^3}} \left(\sqrt[4]{72} + \sqrt[4]{\frac{8}{9}} \right) \right] + 2\frac{H l_{\text{e}} \mu l_y}{k} \left(\frac{j}{FZS} \right)^2 \tag{2.35}$$

To simplify the Equation (2.35), l_{e} is assumed to be half the feedback channel width, $l_{\text{e}} = \frac{l_{\text{f}}}{2}$:

$$P_{\text{tot}} = j^2 l_y \sqrt{\frac{H^3}{FZ}} \left[\sqrt[4]{\frac{\mu}{S^2\kappa^3}} \left(\sqrt[4]{72} + \sqrt[4]{\frac{8}{9}} \right) \right] + j^2 l_{\text{y}} \sqrt{\frac{H^3}{k^3 (FZS)^5}} \sqrt[4]{72\kappa\mu^5} \tag{2.36}$$

Equation (2.36) depends on the KOH concentration for μ, κ [27] and S, and the electrode permeability k, the rest of the variables are constant. The equation can be further simplified to:

$$P_{\text{tot}} = C \left[\sqrt[4]{\frac{\mu}{S^2\kappa^3}} + \frac{3}{4} \frac{\sqrt[4]{\kappa\mu^5}}{(FZ)^2 \sqrt{k^3 S^5}} \right] \tag{2.37}$$

With $C = \frac{4j^2 l_y}{3} \sqrt{\frac{H^3}{FZ}}$, independent of the electrolyte concentration. A plot for the power dissipation as a function of the KOH concentration for different values of the electrode permeability is given in Fig. 2.5. The power dissipation is normalized by dividing the minimum power dissipation, to show the increase in power dissipation when deviating from the ideal KOH concentration:

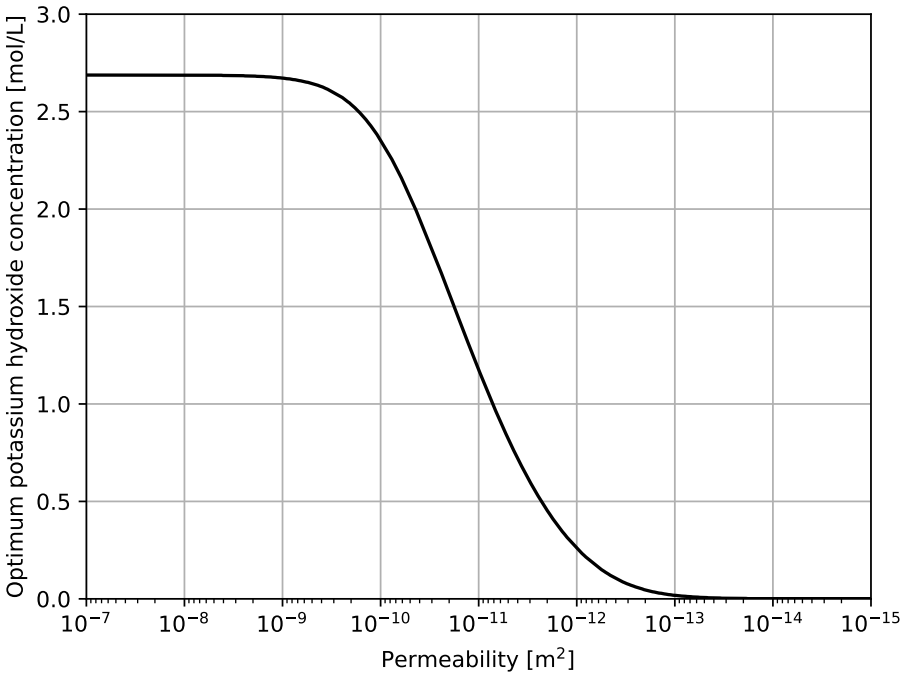

Figure 2.5: Equation (2.37) divided by constant C at different potassium hydroxide concentrations

The figure shows that the second term of Eq. (2.37) can be neglected for permeabilities above 10^{-9} m^2. For lower permeabilities ($k \lesssim 10^{-9}$ m^2), the optimum concentration shift to lower values,

because the viscosity starts to dominate the power dissipation, and the power dissipation increases more drastically when deviating from the ideal concentration. For low permeabilities, Eq. (2.37) can be reduced to the much simpler form:

$$P_{\text{tot}} = C\sqrt[4]{\frac{\mu}{S^2\kappa^3}} \qquad \text{for } k \lesssim 10^{-9}\ \text{m}^2 \tag{2.38}$$

In the next two figures, the KOH concentration for the lowest power dissipation and the fraction of the power dissipation to the pressure drop across the electrode.

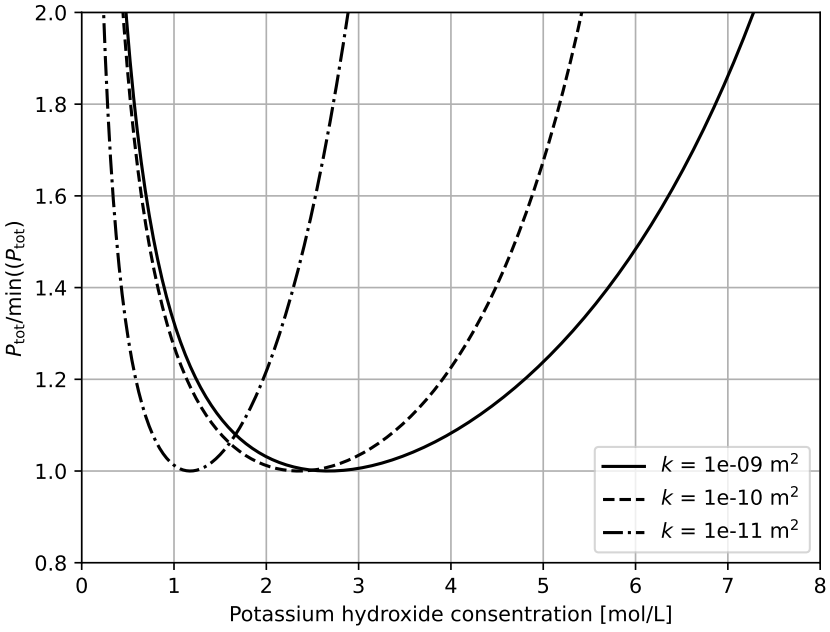

(a) Optimum KOH concentration as a function of electrode permeability

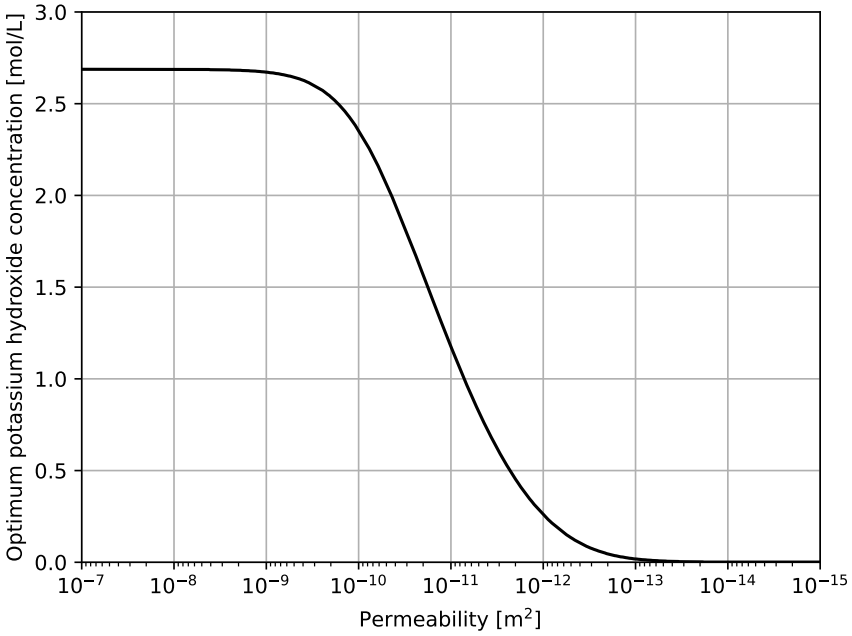

(b) Fraction of the power dissipation due to the pressure drop over the electrode as a function of electrode permeability

Figure 2.6: The dependency of permeability on the optimum KOH concentration and the power dissipation

From these two figures, it can be concluded that the pressure drop across the porous electrodes can be neglected for permeabilities higher than 10^{-9} m^2. For a perforated plate k is roughly $\frac{l^2}{12}$, therefore if the holesize is bigger than ~ 100 μm the pressure drop across the electrodes is negligible. In the case of the used electrode material, the permeability is estimated to be $k = \frac{40 \cdot 10^{-6}}{12} \approx 10^{-10}$ m^2. For this permeability, the theoretical optimum hydroxide concentration is 2.4 mol/L, which is a lot lower than the

commonly used 30 wt% KOH, which is around 6.1 M.

2.6. Flow velocity Limitations

For the design, the flow needs to remain laminar. If the flow gets turbulent, the flow will become chaotic, possibly causing the mixing of hydrogen and oxygen in the feed channel. In addition, turbulence increases the pressure drop in the system and, thus, decreases efficiency. The flow transition between two parallel plates has been documented by Whan et al. [38]. Turbulent effects start taking place at Reynolds numbers above 1400 based on the inter-plate distance. Therefore, this is set as the limit for the Reynolds number in the feed channel. Using equation (2.17) and $\mathrm{Re} = \rho \frac{w_f(0) l_f}{\mu}$, the following relation for the Reynolds number is obtained:

$$\mathrm{Re} = 2\rho \frac{jH}{\mu F Z S} \tag{2.39}$$

The Reynolds number is linearly dependent on the height of the electrode and the current density. High current densities are favourable for the capital cost of an electrolyzer, thus minimizing the height, will be beneficial according to Eq. (2.39). If the flow velocity is limited by a maximum Reynolds number of 1400, the maximum achievable current density can be calculated using Eq. (2.39). The current density as a function of the electrode height for this maximum Reynolds number is shown below:

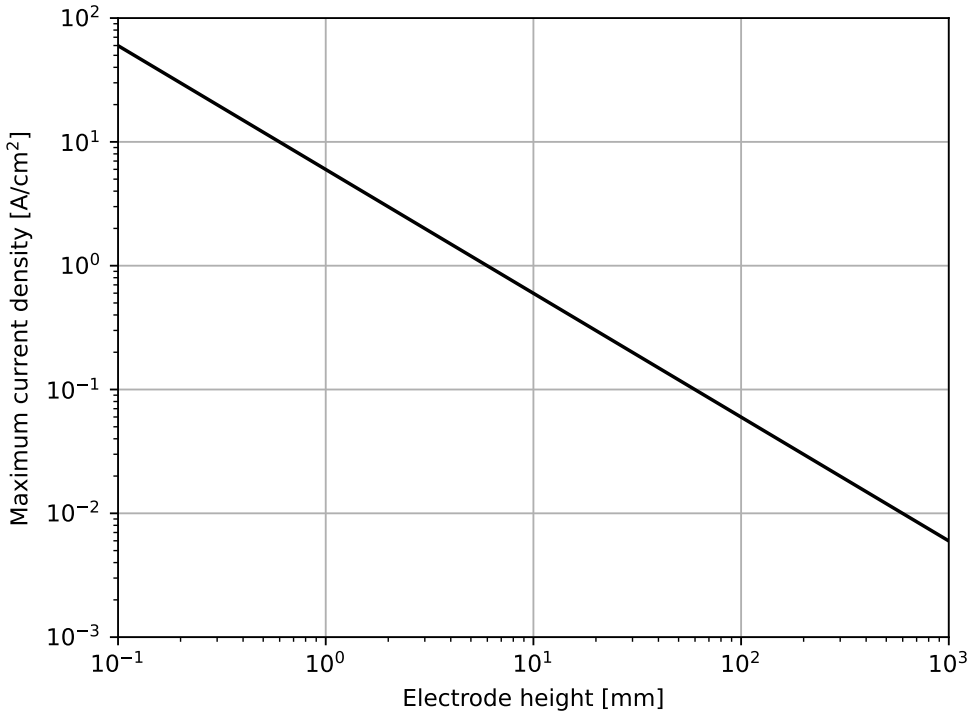

Figure 2.7: Current density when operating at a Reynolds number of 1400 between the electrode as a function of electrode height using 1M KOH electrolyte

3

Methods

The experiments were conducted using a setup which is schematically illustrated in Fig. 3.1. The flow is driven by a magnetic drive regenerative turbine pump, HTP-B, from March May Ltd. Using ball valve 'V1', the bypass can be opened and closed, thereby controlling the flow rate through the electrolyzer. Valve 'V2' is the proportional solenoid valve, 239080, 2 port(s) , NC, 24 V dc, 1/4in, from Bürkert Fluid Control Systems. Using a PWM signal the valve can be operated at various positions allowing more precise fluid control. The flow rate was measured using the flow sensor, 'FS', and the pressure drop over the cell was measured with sensors 'P1' and 'P2'. These sensors were bought from TinyTronics, with the flow sensors being the YF-S401 Water Flow Sensor and the pressure sensor the HK1100C Water Pressure Sensor - 0-12bar - G1/4". The pressure was measured at the inlet of the electrolyzer and the outlet of the cathode side. The tubing was 1/4 inch silicon tubing, which was chosen due to minimize pressure drop. Using the Hagen-Poiseuille equation ($\frac{\Delta p}{L} = \frac{8\mu Q}{\pi R^4}$) at standard conditions with a 26 mL/s flow rate, the pressure drop is 0.65 bar/m, which was deemed to be low enough to run the experiments.

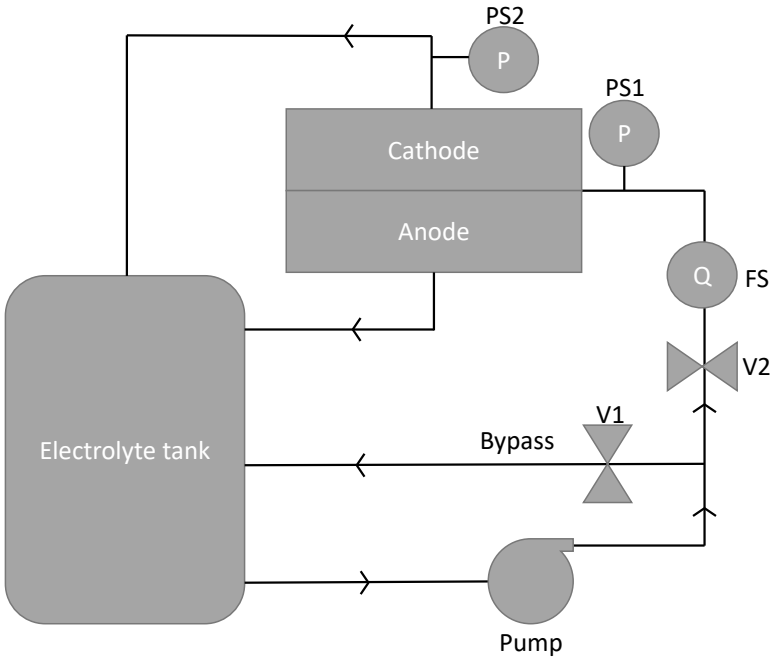

Figure 3.1: Schematic of the used setup for the experiments. The arrows denote the flow direction. The annotations are V1: Ball valve; V2: Proportional solenoid valve; FS: Flow rate sensor; P1: Inlet pressure sensor; P2: Outlet pressure sensor

The real test setup is shown in Fig. 3.2.

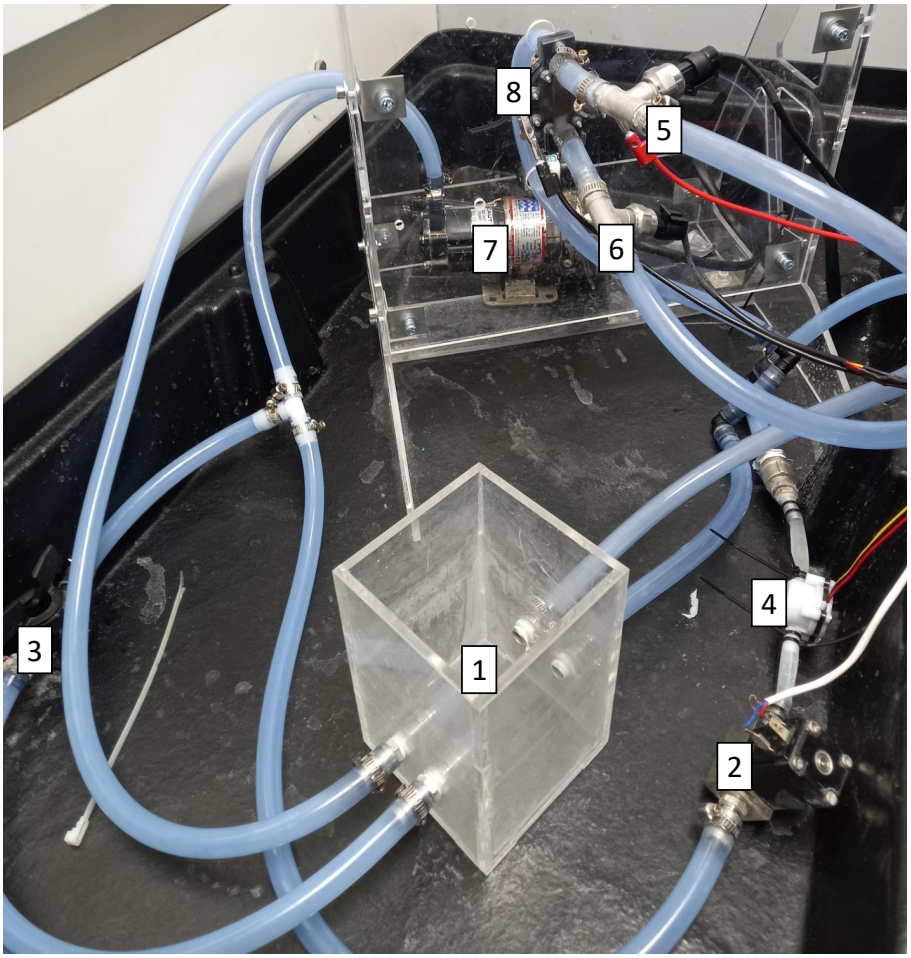

Figure 3.2: The setup used in experiments for the experiments with annotations: 1: Electrolyte tank; 2: Proportional solenoid valve; 3: Ball valve; 4: Flow rate sensor; 5: Outlet pressure sensor; 6: Inlet pressure sensor; 7: Pump; 8: electrolyzer.

3.1. Electrolyzer

The electrolyzer housing was built using the Formlabs 3B SLA 3D printer. This printer is capable of 3D printing necessary for the complex geometry and the resin, Formlabs Clear Resin V4, is resistant to KOH. The gaskets are made of laser-cut 0.5mm thick EPDM rubber. The whole stack was clamped using bolts. The electrodes are the VECO ZP200617 nickel plate. This is a 300-micron thick plate with a 12 % open area. The holes in this electrode are slot-shaped holes with a dimension of 170-micron length and 40-micron height. In the electrolyzer, the dimensions of the used electrode area are 9 x 18.8 mm.

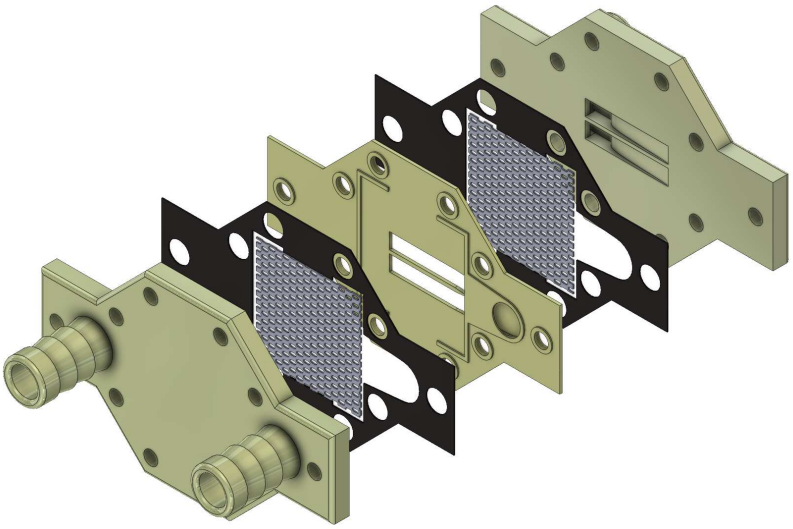

Figure 3.3: Exploded view of the electrolyzer on its side. From left to right: Product outlet (top left tube), Electrolyte inlet (bottom right tube) endplate with the variable feed channel inside at the inner side facing away from the camera; EPDM Rubber gasket (black) and nickel electrode (metallic); Feed channel plate; EPDM Rubber gasket (black) and nickel electrode (metallic); Product outlet endplate with the variable feed channel inside at the inner side facing towards from the camera

Figure 3.3 shows the two endplates containing the variable feed channel in the middle of the flat side of the plate. These plates have 3D-printed hose pillars to connect the electrolyzer to the flow setup using silicon tubing. The electrolyte enters one of the tube pillars where it flows to the feed channel plate. Through a narrow channel, it enters two large rectangular holes which are aligned with the variable feed channel. The electrode is sandwiched between the endplate and the feed channel plate. A picture of the assembled electrolyzer in Fig. 3.3 is shown in the following figure:

Figure 3.4: Assembled electrolyzer on its side with the silicon tubes connected. The exploded view of this electrolyzer's 3D render is shown in Fig. 3.3

3.2. Lab Experiments

The experiments in the lab consist of comparing a specific state of the system with the base case, which is an 0.8 mm gap with a straight discharge channel and a 1M KOH solution.

The straight discharge channel made it possible to insert a perspex window, enabling filming the back of the electrodes, which was not possible with the variable discharge channel due to its complex form and the poor transparency of the resin. The experiments consist of making IV curves, which were generated using a power supply. The used power supply is the programmable OWOWN SPE6103. Using a Python script combined with SCPI language the electrolyzer could be supplied with discrete potential steps. The experiments were run between 0 v and 5 V and between 1 V and 9 V, with 100 data points. Each test lasted around 10 seconds, to minimize hydrogen and oxygen production. This was to prevent the electrolyzer from creating excessive gas which could potentially cause the electrolyzer of filling with gas. During this research, 4 different experiments have been carried out, each varying a certain parameter, shown in Table 3.1.

Table 3.1: Different experiments performed to evaluate the performance of the electrolyzer

Name of the experiment	Variable of interest	Change in setup
Inter-electrode gap	l_{f}	0.6 mm, 0.8 mm, 1.5 mm
KOH concentration	c_{KOH}	1M, 6M
Degassing	S	From degassed state towards saturated state
Discharge channel	l_d	Straight geometry, Variable geometry

All lab experiments except for the discharge channel geometry experiment have been filmed using a 60fps 4MP microscope camera. The cathode side was filmed to see the effect of the different current densities on the mass transport of bubbles and to see what the effect of keeping the gasses saturated was.

To see the effect of the saturation on the electrolyte on the resistance due to bubble formation, the gasses in the electrolyte first needed to be expelled. The degassing was done using a vacuum chamber from Vevor. After a minute under a 5 kPa vacuum, which expels most of the gasses in the electrolyte [39], the electrolyte was assumed to be degassed.

4

Numerical study

To calculate the optimum discharge channel geometry, numerous assumptions have been made. In this section, the geometry together with the assumptions will be verified using COMSOL's free and porous flow model. The flow rate is chosen so that the flow is laminar because turbulence (Re > 1400) causes the mixing of hydrogen and oxygen in the feed channel.

The goal of this COMSOL study is listed below:

- Comparing the variable discharge channel geometry with a conventional, straight discharge channel
- Investigating the effect on the uniformity of the flow across the electrodes of inlet velocity and the permeability of the electrode
- Investigating the effect of the cut-off height, $\hat{z}_{\text{co}}$, on the performance of the variable discharge channel geometry

4.1. Comparing the improved discharge channel geometry to the straight geometry at various velocities

The uniformity of the flow through the electrode is evaluated by the ratio between the modelled flow and the ideal case, called the normalized velocity. In the ideal case, the electrolyte flows uniformly through the electrode with a velocity of $U_{\text{i}} = w_{\text{f}}(0)\frac{l_{\text{f}}}{2H}$. The normalized velocity can be calculated by taking the modelled velocity and dividing it by the ideal velocity:

$$\overline{U}(z) = \frac{U_{\text{m}}(z)}{U_{\text{i}}} \tag{4.1}$$

If $\overline{U}(z) = 1$ the modelled velocity is identical to the ideal velocity. When $\overline{U}(z) < 1$ the flow velocity is locally lower than the ideal case and this will lead to potentially insufficient hydrogen removal at the electrode, meaning bubbles will emerge.

Fluid variables

The fluid variables will be chosen for 2.4 M KOH, which is the optimal KOH concentration according to Fig. 2.5. The electrolyte is modelled at room temperature (25 °C) and atmospheric pressure. The fluid variables used in the study together with their references are presented below:

Table 4.1: Fluid constants of a 2.4 M KOH solution at atmospheric pressure and room temperature

Constant	description	Value	Reference
κ	Ionic conductivity	0.46 S/cm	Gilliam et al. [27]
μ	Dynamic viscosity	1.0 mPa s	Kuznetsov et al. [36]
ρ	Density	$1.1 \cdot 10^3$ kg/m^3	Gilliam et al. [27]
S_{V}	solubility	8.1 mL H_2/L H_2O	Ruetschi et al.[37]
ρ_{H_2}	Specific density of hydrogen	41 mol/m^3	NIST [40]

The solubility of hydrogen can be expressed in mol/m^3: $S = S_{\mathrm{V}} \cdot \rho_{\mathrm{H_2}} = 0.33$ mol/m^3

The uniformity of the flow depends on the inlet velocity and the permeability of the flow. A higher inlet velocity means that the flow will overcome the hydraulic resistance in the feed channel more easily due to the increased inertia. A high permeability will decrease the pressure build-up in the feed channel. To better understand the balance between pressure drop and inertia, the Euler number can be used:

$$\mathrm{Eu} = \frac{\Delta p}{\frac{1}{2}\rho w_{\mathrm{f}}(0)^2} \tag{4.2}$$

Δp can be expressed in the pressure drop in the feed channel described by Hagen-Poiseuille and the pressure drop across the electrode, described by Darcy,

$$\Delta p = \mu w_{\mathrm{f}}(0) \left(6\frac{H}{{l_{\mathrm{f}}}^2} + \frac{l_{\mathrm{e}} l_{\mathrm{f}}}{2Hk} \right) \tag{4.3}$$

Therefore, the Euler number is,

$$\mathrm{Eu} = \frac{\mu}{\rho w_{\mathrm{f}}(0)} \left(12\frac{H}{{l_{\mathrm{f}}}^2} + \frac{l_{\mathrm{e}} l_{\mathrm{f}}}{Hk} \right) \tag{4.4}$$

The Euler number increases when the inlet velocity or the permeability is low. A high Euler number means that the flow is dominated by hydraulic resistances rather than inertia.

Before the results are shown, the two geometries are presented with their labelled regions:

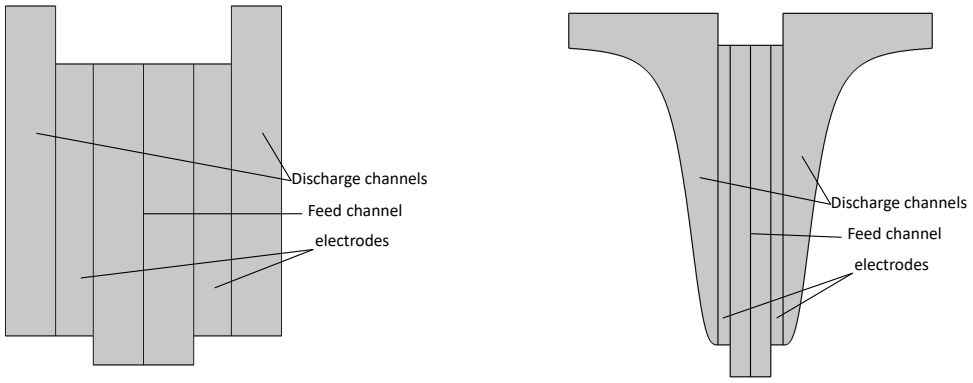

(a) Straight discharge channel geometry

(b) Variable discharge channel geometry

Figure 4.1: The two geometries used in the CFD simulations with the labelled regions

4.2. Velocity

In the next figure, the velocity across the electrodes is measured as a function of the height in the feed channel. The permeability remains constant at 10^{-10} m^2, which is the estimated permeability of the electrodes. Using the fluid constants in Table 4.1 in Eq. (2.39), the maximum velocity is calculated to be 1.6 m/s to keep the flow below a Reynolds number of 1400.

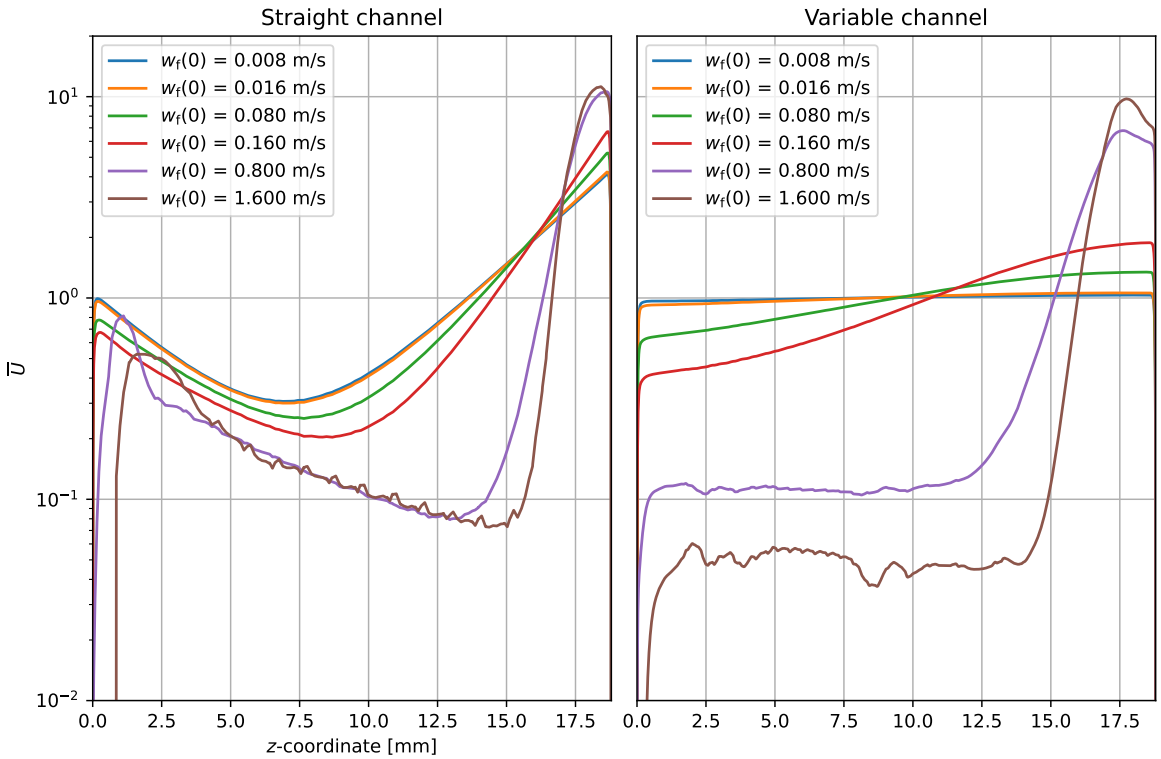

Figure 4.2: Normalized velocity of the straight discharge channel and the variable discharge channel with an electrode permeability of 10^{-10} m^2 as a function of the z-coordinate in the feed channel for various inlet velocities. At $w_f(0) = 1.6$ m/s the flow field start showing noise because it gets close to turbulence

The Euler numbers are documented in the table below:

Inlet velocity	Euler number
0.008 m/s	55
0.016 m/s	27
0.08 m/s	5.5
0.16 m/s	2.7
0.8 m/s	0.55
1.6 m/s	0.27

Table 4.2: The Euler number for the velocities in Fig. 4.2

The variable discharge channel case shows that it approaches the ideal velocity ($\overline{U} = 1$) for Euler numbers higher than 1. The Straight discharge channel case never approaches this ideal velocity. Both cases seem to become inhomogeneous at around Eu < 1. The pressure drop and streamline plots also show this:

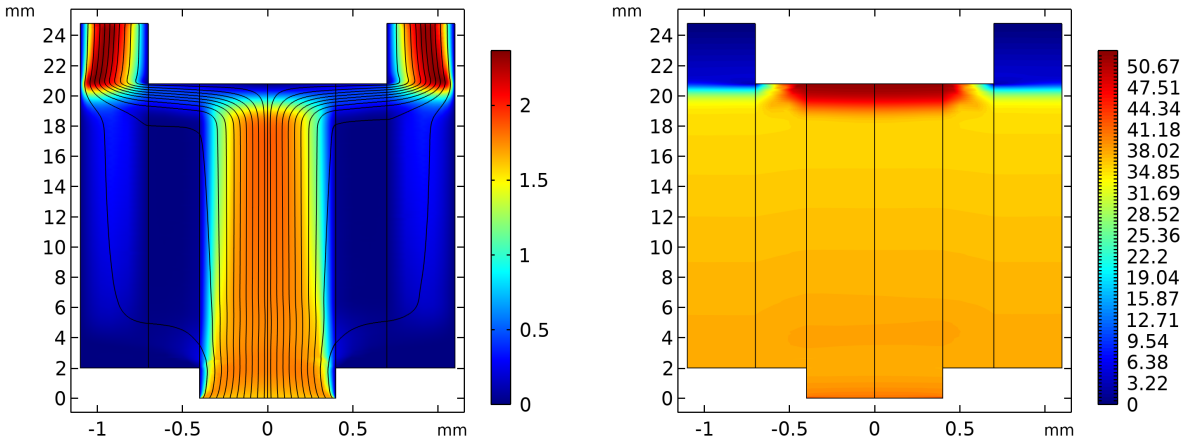

(a) Velocity plot with streamlines, the colour bar has units m/s

(b) Pressure plot, the colour bar has units mbar

Figure 4.3: Velocity and pressure plots of the straight discharge channel case with an inlet velocity of 1.6 m/s and a permeability of 10^{-10} m^2

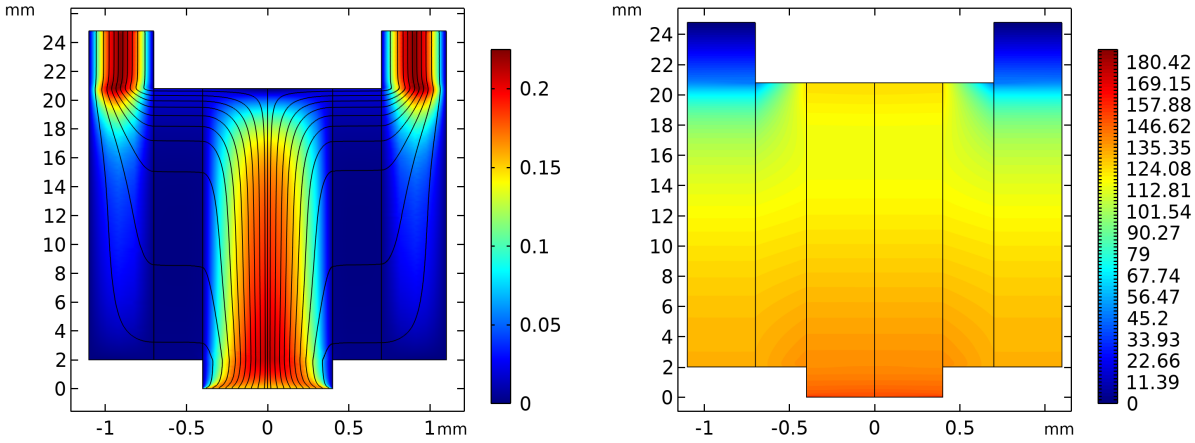

(a) Velocity plot with streamlines, the colour bar has units m/s

(b) Pressure plot, the colour bar has units Pa

Figure 4.4: Velocity and pressure plots of the straight discharge channel case with an inlet velocity of 0.16 m/s and a permeability of 10^{-10} m^2

The 1.6 m/s velocity case in Fig. 4.3b shows that the pressure can not build up in the feed channel due to its high inertia. The flow hits the top end of the feed channel, like a water jet on a plate. Decreasing the flow seems to make the flow more uniform across the electrodes, as the streamlines spread more out in Fig. 4.4a and the pressure builds up more seen in Fig. 4.4b. However, there most streamlines still pass the electrodes at the top. The variable feed channel has better uniformity across the electrodes, as seen in the streamline plot:

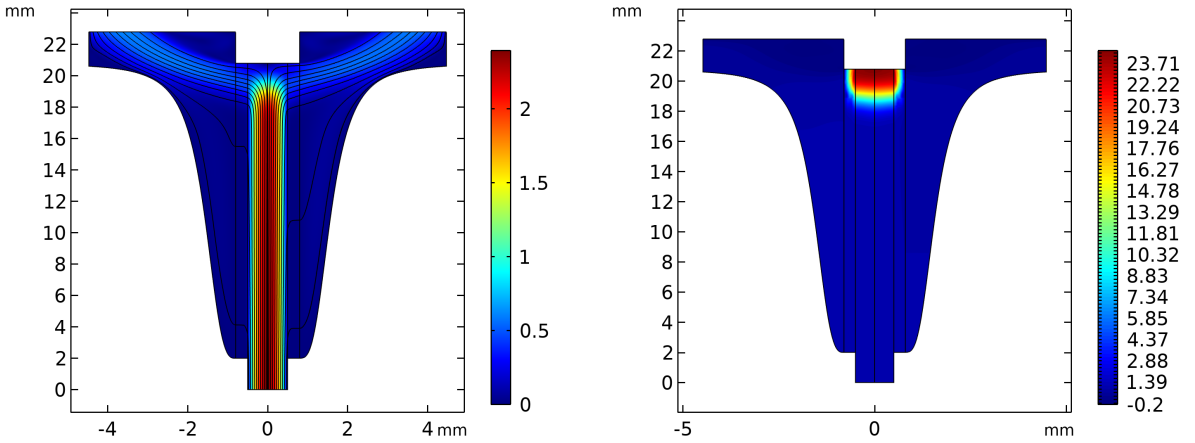

(a) Velocity plot with streamlines, the colour bar has units m/s

(b) Pressure plot, the colour bar has units mbar

Figure 4.5: Velocity and pressure plots of the variable discharge channel case with an inlet velocity of 1.6 m/s and a permeability of 10^{-10} m^2

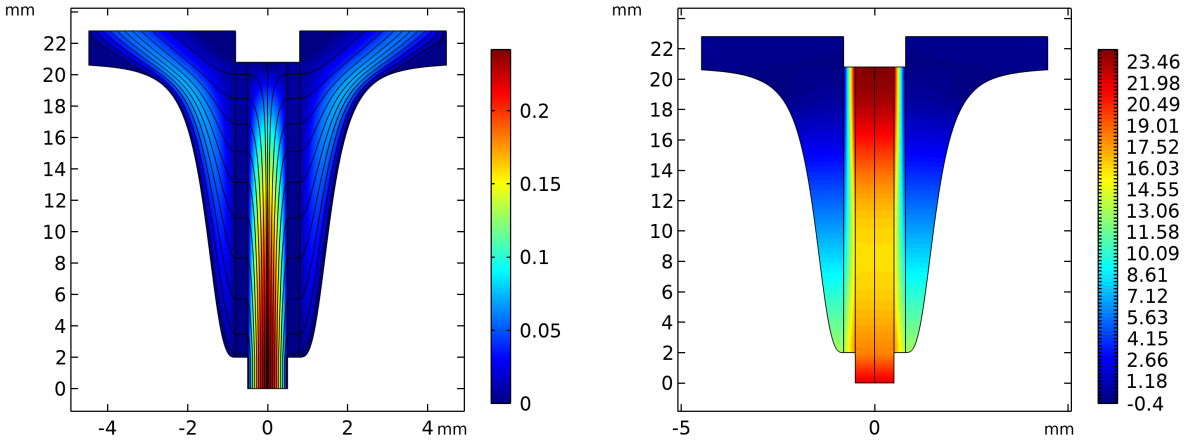

(a) Velocity plot with streamlines, the colour bar has units m/s

(b) Pressure plot, the colour bar has units Pa

Figure 4.6: Velocity and pressure plots of the variable discharge channel case with an inlet velocity of 0.16 m/s and a permeability of 10^{-10} m^2

The variable feed channel distributes the flow uniformly in the 0.16 m/s case, which is shown in Fig. 4.6a. Here, the pressure drop of the variable discharge channel is considerably lower than that of the straight discharge channel. Ignoring the exit effects, the straight discharge channel has a pressure drop of 50 Pa, while the variable discharge channel has a pressure drop of roughly 20 Pa. The 1.6 m/s variable feed channel case in Fig. 4.5 has the same problems as with the straight channel where the flow cannot build up pressure in the feed channel and leaves primarily at the top of the channel. In this case, the pressure drop is equal for the variable and the straight channel, with an overall pressure drop of around 20 mbar, if the exit effects are ignored.

4.3. Permeability

In Fig. 4.7, the effect of permeability on the uniformity of the flow is investigated. The inlet velocity is kept at 0.16 m/s because the Comsol model did not converge for higher inlet velocities with low electrode permeability ($k < 10^{-9}$ m^2).

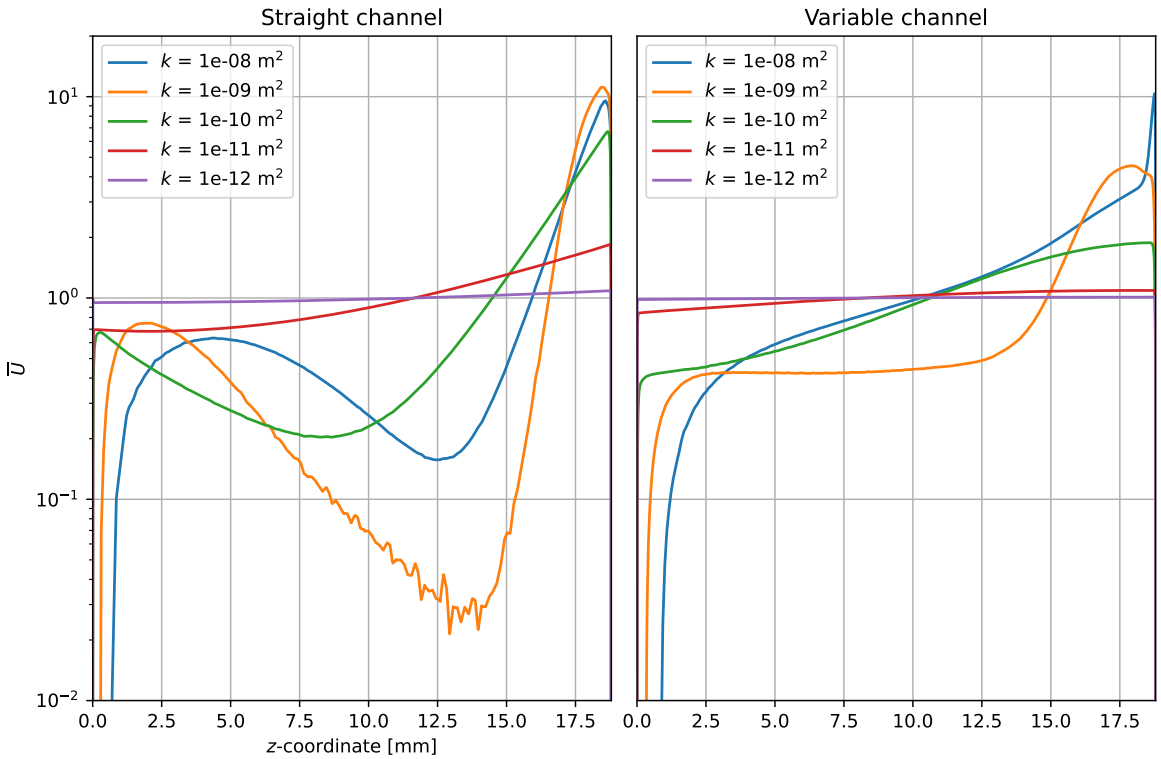

Figure 4.7: Normalized velocity of the straight discharge channel and the variable discharge channel with an inlet velocity of 0.16 m/s as a function of the z-coordinate in the feed channel for electrode permeabilities.

The Euler numbers are documented in the table below:

Table 4.3: The Euler number for the permeabilities in Fig. 4.7

Electrode permeability	Euler number
10^{-8} m^2	2.0
10^{-9} m^2	2.1
10^{-10} m^2	2.7
10^{-11} m^2	9.3
10^{-12} m^2	75

In Fig. 4.7, both discharge channel cases approach the ideal velocity at Eu > 10. For the variable feed channel case the flow velocity stays between 20 % of the ideal velocity. This is because, with a decreased permeability, the pressure drop across the electrodes is much bigger than the pressure drop in the feed channel and the inertia of the flow. This makes the flow distribute evenly across the membrane. This is also observed in the streamline and pressure plot in Fig. 4.8.

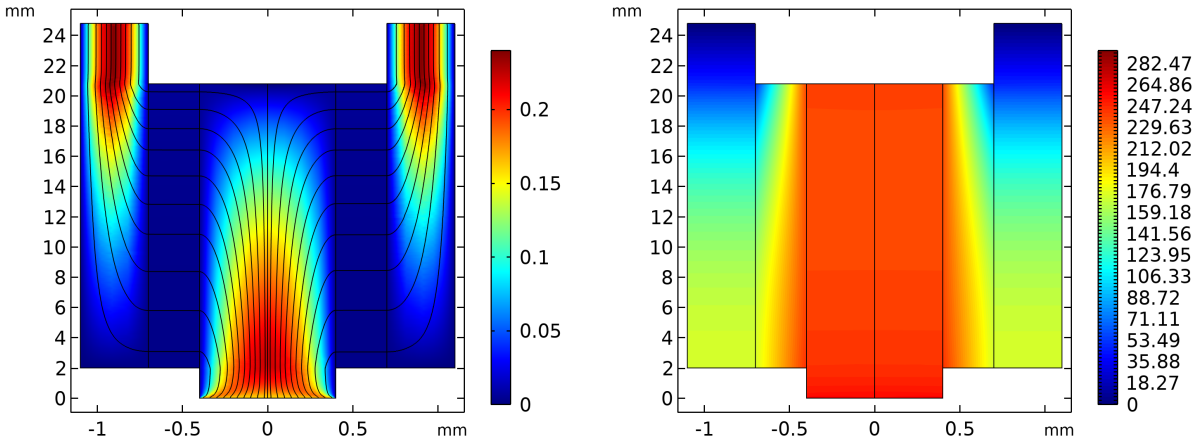

(a) Velocity plot with streamlines, the colour bar has units m/s

(b) Pressure plot, the colour bar has units Pa

Figure 4.8: Velocity and pressure plots of the straight discharge channel case with an inlet velocity of 0.16 m/s and a permeability of 10^{-11} m^2

This indeed shows that the uniformity with the decreased permeability is even better than in Fig. 4.4. The streamlines now spread out over the whole height of the feed channel. However, this comes at the cost of a high pressure drop across the electrodes, seen in Fig. 4.8b.

4.4. Dependency of cut-off height

The cut-off height is an important parameter in the design. The cut-off height may not be chosen too large, as the design will stretch far outwards in the x-direction, increasing the size of the electrolyzer and, therefore, capital cost. The cut-off height needs to be minimized without disturbing the uniformity of the flow across the electrodes. The electrolyzer was modelled with a permeability of 10^{-10} m^2 and an inlet velocity of 0.16 m/s. Figure 4.9 describes the flow field across the electrodes as a function of the height for various cut-off heights

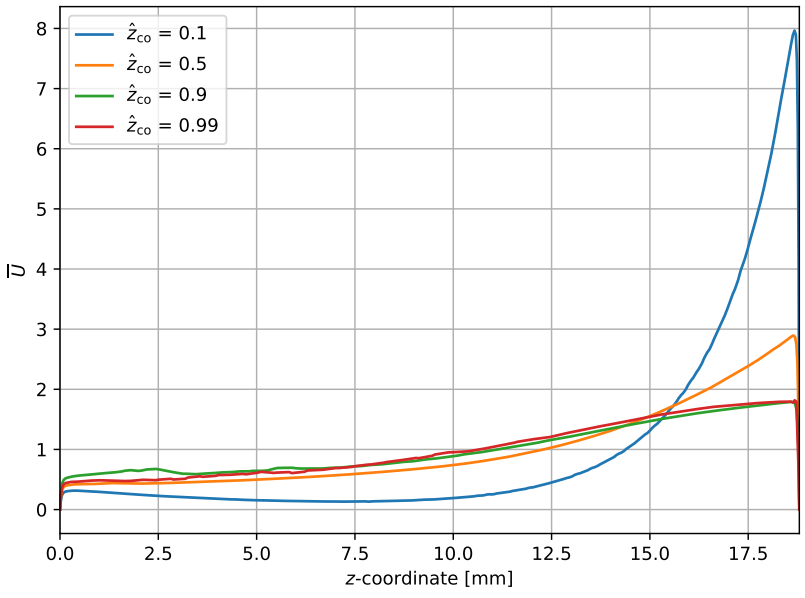

Figure 4.9: Normalized velocity across the electrodes with an inlet velocity of 0.16 m/s as a function of the z-coordinate for various cut-off heights

There is a clear relation between the cutoff height and the uniformity if the flow. The lower the cut-off height becomes, the more the flow begins to shape like it had a straight discharge channel. Lowering

the inlet velocity to 0.016 m/s makes this effect stronger and increasing the inlet velocity to 0.8 m/s makes this effect weaker, which is shown in Fig. 4.10.

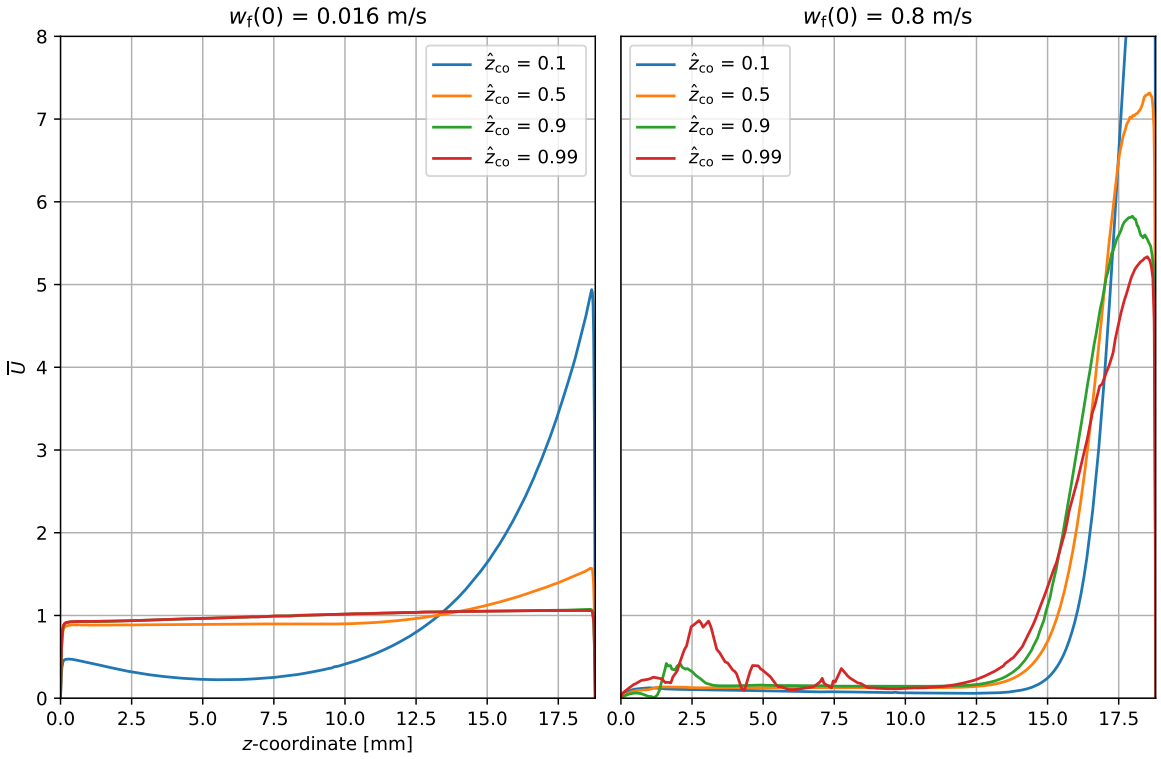

Figure 4.10: Normalized velocity across the electrodes with an inlet velocity of 0.016 m/s in the left graph and 0.8 m/s in the right graph as a function of the z-coordinate for various cut-off heights. The flow at the $W_f(0) = 0.8$ m/s case shows noise due to the high flow rate.

Figure 4.11 shows that changing the permeability has a much smaller effect on the difference in cut-off height.

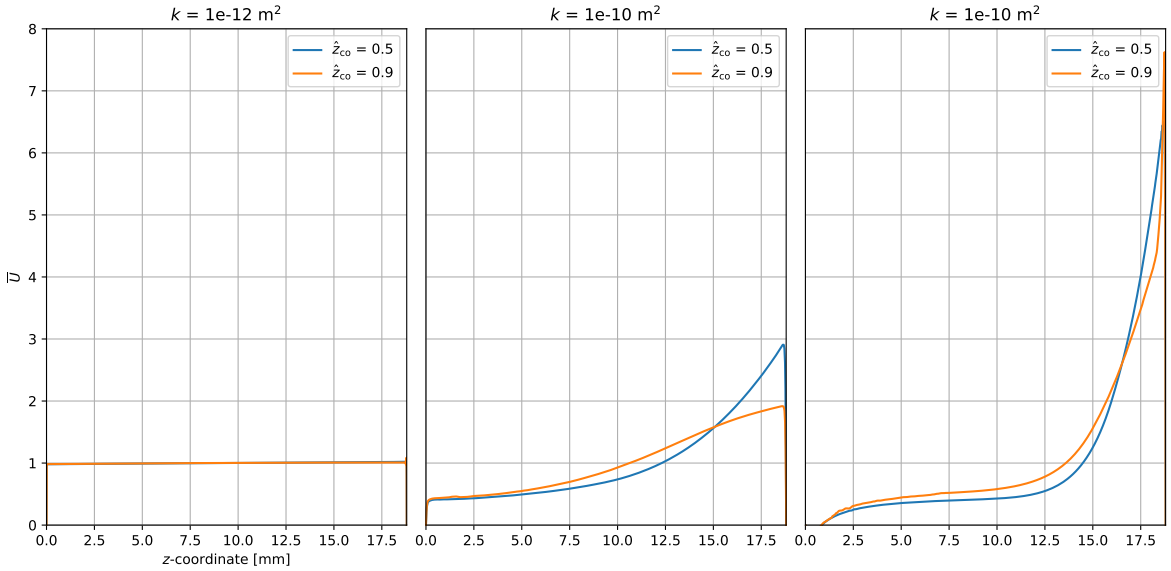

Figure 4.11: Normalized velocity across the electrodes with an inlet velocity of 0.16 m/s a function of the z-coordinate for various cut-off heights. In this case, the permeability is changed, which shows a smaller effect than in the case of changing the velocity, shown in Fig. 4.10

5

Experimental results

The result section documents the effect on electrolyzer performance of changing various parameters. This section is subdivided into multiple subsections, each showing the effect of one of the different design parameters listed in chapter 3 (Method). Each experiment will be compared to the base case unless denoted otherwise, which is a 0.8 mm electrode gap with a straight discharge channel and 1 molar KOH. The other electrolyzer's geometrical constants are shown in the table below:

Name	Variable	Value
Channel depth	l_y	9 mm
Heigth of the channel	H	18.8 mm
Electrode thickness	l_e	0.3 mm
Electrode area	A	1.69 cm^2

Table 5.1: Geometrical constants in the electrolyzer design

The flow rates are expressed in mL/s but can be converted to cm/s by dividing the flow rate by the desired area, for example, $U = 13/1.69 = 7.7$ cm/s superficial flow velocity across the electrodes with an inlet flow rate of 26 mL/s (half the inlet flow rate for each electrode).

5.1. Inter-electrode gap

The different gaps in the inter-electrode gap experiments are a 0.6 mm, 0.8 mm and 1.5 mm gap, meaning the area of the feed channel is 0.054 cm^2, 0.072 cm^2 and 0.135 cm^2 for the respective gaps. The performance of each experiment was measured by comparing the total power dissipation at different flow speeds and current densities. First, the IV curves are shown for the three different inter-electrode gaps. The 1.5 mm gap was tested at lower current densities because it has a higher resistance than the rest of the configurations and thus has the possibility to heat the electrolyte, which could cause a discrepancy in the result.

5.1.1. IV curves

The IV curves for the 3 gaps at various flow rates are shown in the figure below:

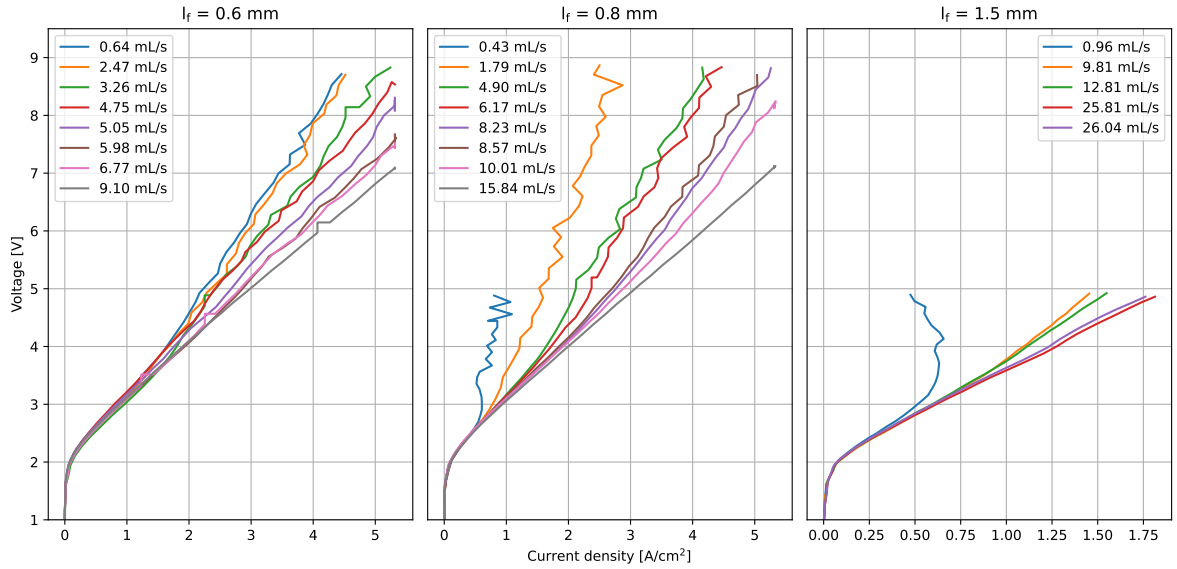

Figure 5.1: IV curves for a 0.6 mm, 0.8 mm and 1.5 mm inter-electrode gap

The 9.10 mL/s and the 6.77 mL/s case of the 0.6 mm gap show some sudden jumps at 2.3 A/cm^2 and 4.1 A/cm^2 respectively. This is due to an error in the power supply and is not physical.

5.1.2. Pressure Drop

The pressure drop at various Reynolds numbers is documented below:

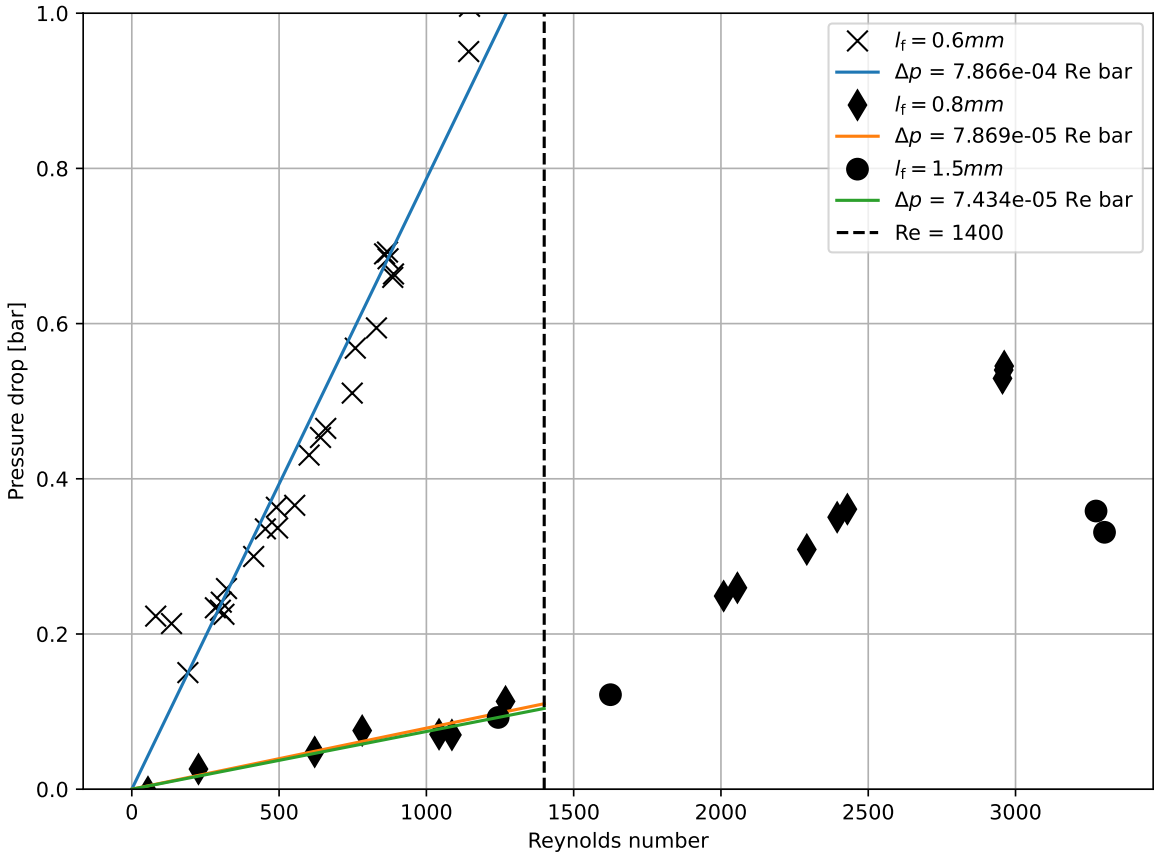

Figure 5.2: Pressure drop at Reynolds numbers of the different inter-electrode gaps

The pressure drop between the 1.5 mm case and the 0.8 mm case is nearly identical below the turbulent transition (Re < 1400). This can be caused by the poor accuracy of the pressure sensor. The pressure drop, of 0.1 bar, in the 0.8 mm case is close to the pressure drop, of 0.2 bar, found in the CFD simulations in Fig. 4.4b. In the 0.6 mm case, the pressure drop is far higher than in the other two gap cases, which again might be due to the poor accuracy of the pressure sensors. The pores in the electrodes are elongated ovals with a 40-micron height and a width of 170 microns. From the theory chapter, it was stated that a hole size bigger than 100 microns. This means that the pressure drop across the electrodes has to be included. The pressure drop can be described using Eq. (2.19) and Eq. (2.22). To compare the theory with the results Eq. (2.19) has to be expressed in terms of the Reynolds number,

$$\Delta p = 6\frac{H\mu^2}{\rho {l_f}^3}\mathrm{Re} + \mu^2\frac{l_e l_f}{Hk}\mathrm{Re} \tag{5.1}$$

The factor $6\frac{H\mu^2}{\rho {l_f}^3}$ can be compared with the factor from the curve fits in Fig. 5.2. The next table shows the curve fits from Fig. 5.2 divided by the factor $6\frac{H\mu^2}{\rho {l_f}^3}$:

Table 5.2: Comparison of the measured pressure drop across the electrolyzer versus the theoretical pressure drop according to Eq. 5.1

Gap width	Ratio
0.6 mm	150
0.8 mm	30
1.5 mm	50

This rather large difference can be explained by pressure losses elsewhere in the system, or by the

poor resolution of the pressure sensors.

5.1.3. Power dissipation

The total power dissipation is calculated as the sum of the pressure and the electrical power dissipation:

$$P_{\text{tot}} = Q\Delta p + jA\phi \tag{5.2}$$

The power dissipation is then divided by the hydrogen production rate to show the energy needed to produce one kilogram of hydrogen. In equation form, this is,

$$E_{\text{H}_2} = \frac{P_{\text{tot}}}{\dot{n} M_{\text{H}}} \tag{5.3}$$

$\dot{n}$ is the rate of hydrogen production in mol/s from Eq. (2.15). ϕ is dependent on the current density, shown in the first section of the theory chapter 2,

$$E_{\text{H}_2} = \frac{Q\Delta p + jA(\phi_{\text{T}} + b\ln(j) + jAR_{\Omega})}{\dot{n} M_{\text{H}}} \tag{5.4}$$

Furthermore, $\dot{n}$ can be substituted with Eq. (2.15),

$$E_{\text{H}_2} = \frac{FZ}{M_{\text{H}}}\left[\frac{Q\Delta p}{jA} + (\phi_{\text{T}} + b\ln(j) + jAR_{\Omega})\right] \tag{5.5}$$

The energy used during experiments is plotted together with the Higher Heating Value (HHV) of hydrogen, which is:

$$E_{\text{HHV}} = \frac{\phi_{\text{T}} FZ}{M_{\text{H}}} \approx 142 \text{ MJ/kg} \tag{5.6}$$

The energy used for hydrogen production during experiments is shown in Fig. 5.3.

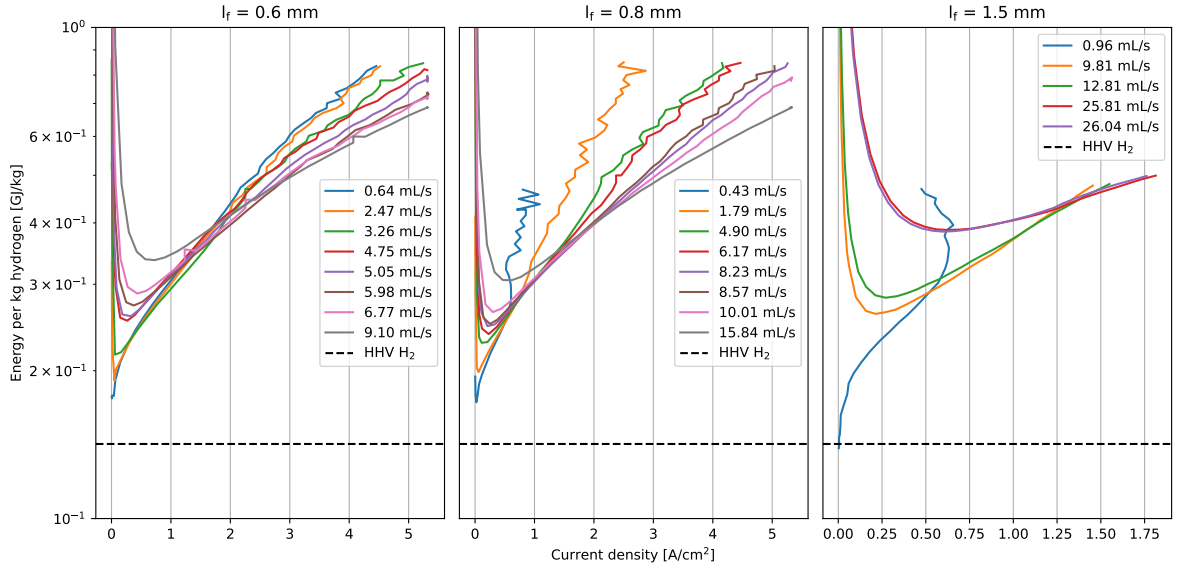

Figure 5.3: The energy per kg produced hydrogen using Eq. (5.5) for various flow rates for the three inter-electrode gaps

The graphs in Fig. 5.3 show that low flow rates give a high efficiency at current densities below 0.5 A/cm^2. At higher current densities the effect of pressure drop is outweighed by the electrical power dissipation. This is described by Eq. (5.5). The 0.6 mm gap and the 0.8 mm gap have very similar efficiencies. This might be caused by the pump not being able to provide a high enough head to overcome the pressure drop in the 0.6 mm gap. The maximum flow rate possible for the 0.6 mm gap was 9.10 mL/s while the 0.8 mm gap could run at 15.84 mL/s. If the approximately same flow rate

is compared for both gaps, which is 9.10 mL/s case of the 0.6 mm gap compared to the 8.57 mL/s case of the 0.8 mm gap, the 0.6 mm gap electrolyzer saves around 160 MJ/kg hydrogen at a current density of 5 A/cm^2. This is due to the reduction in the inter-electrode gap, causing a reduction in ohmic resistance.

5.1.4. Transition current density

Figure 5.1 shows that the IV curves start to deviate to a regime with higher resistance. This transition is dependent on the flow rate of the system and is from now on called the transition current. The next figure shows the flow rate at which the transition in resistance occurs against the current density.

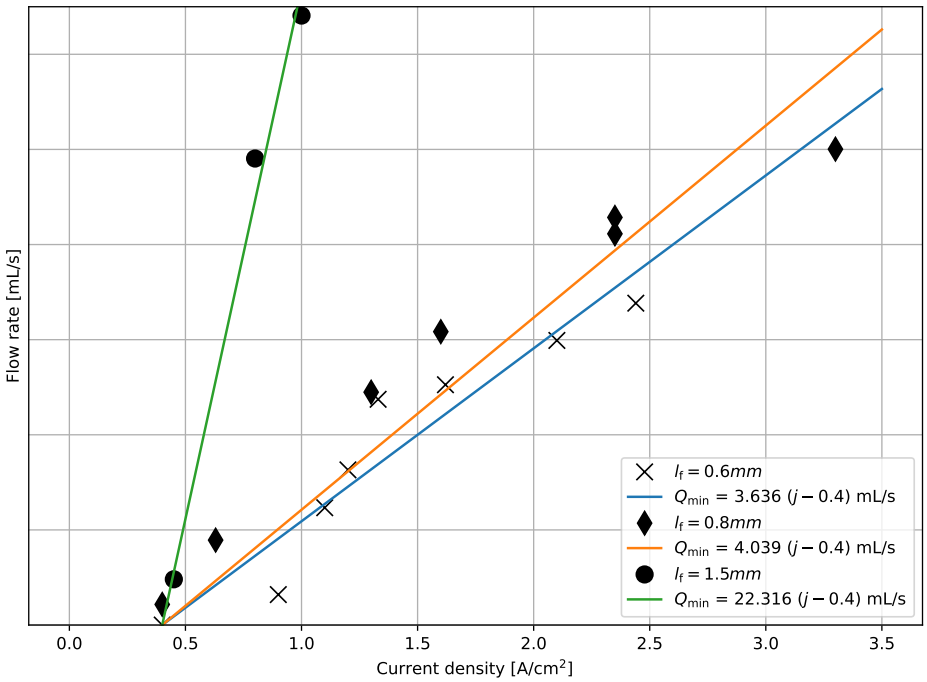

Figure 5.4: Transition current density, the current density where the resistance due to bubbles starts to be noticeable, as a function of flow rate for the gaps. Each data set for a specific gap is followed by a curve fit where j is in A/cm^2.

Figure 5.4 shows that the relation between transition current and flow rate does not intersect the origin, but rather has an offset starting around 0.4 A/cm^2. This means that without flow it is possible to run the electrolyzer at a current density below 0.4 A/cm^2, which is potentially possible due to the natural convection created by the bubbles. The exact current density for which the linear fit intersects the x-axis is hard to determine but seems to be the same for each gap. Therefore the offset for the linear fit will be assumed to be 0.4 A/cm^2 for all cases. Contrary to the theoretical equation, Eq. (2.16), the transition current densities seem to show a lower order dependence on flow rate. In the rest of this research, the fits will follow a linear relation to be able to compare them to Eq. (2.16).

5.1.5. Bubble shear

In the theory section, it was determined that the transition current was governed by the amount of flow crossing the electrodes. This may be a faulty hypothesis because in Fig. 5.5 a clear influence of the electrode gap on the transition current of the electrolyzer is observed. Although the electrode gap does not have an influence on the superficial velocity across the electrodes, due to the conservation of mass, it is possible to conclude that the transition current density is not determined by the flow across the electrodes. Instead, a hypothesis is that the bubble resistance onset concentration is determined by the shear rate close to the wall. This could give an indication of the residence time of bubbles at the electrode surface inside the feed channel. Assuming a fully developed flow between the electrodes, the shear rate at the wall is determined by the following equation:

$$\dot{\gamma} = 6\frac{Q_{\text{min}}}{l_y {l_f}^2} \tag{5.7}$$

Using the values for Q_{min} from Fig. 5.4 the equation for shear rate can be filled in to obtain Table 5.3. For convenience, the current density is chosen to be 1.4 A/cm^2, which gives the slope for each of the curves fits from Fig. 5.4.

Table 5.3: Shear rate at the wall using the necessary flow rate for a transition current of 1.4 A/cm^2 inserted equation (5.7)

Gap width	Flow rate	Shear rate
0.6 mm	3.636 mL/s	$6.7 \cdot 10^4$ s^{-1}
0.8 mm	4.039 mL/s	$4.2 \cdot 10^4$ s^{-1}
1.5 mm	22.316 mL/s	$6.6 \cdot 10^4$ s^{-1}

The three shear rates are of the same order size hinting that the hypothesis might be correct. However, to substantiate this hypothesis more data points have to be acquired.

5.1.6. Effect of solubility

In the chapter 2 (Theory), the relation between the minimum required flow rate for saturation and current density was established. The equation yields,

$$Q_{\text{th}} = 2\frac{jA}{FZS} \tag{5.8}$$

Comparing this theoretical relation from Eq. 5.8 with the flow rate where the transition to a higher resistance occurs in the experiments, results in the following graph:

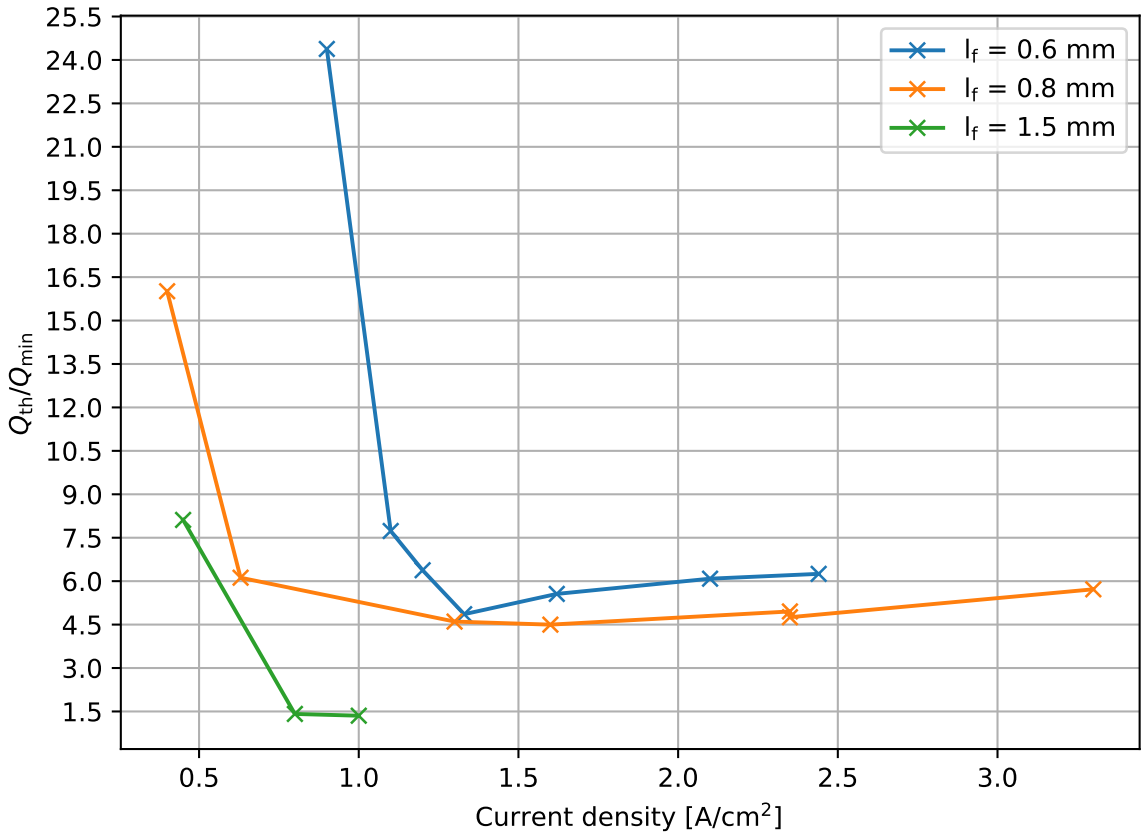

Figure 5.5: The theoretical needed flow rate for saturation of gasses divided by the transition flow rate, $Q_{\text{th}}/Q_{\text{min}}$

From this graph, it becomes clear that the bubble resistance onset concentration is not just limited by the solubility of hydrogen in the electrolyte. The three plots in Fig. 5.5 show that the difference between theory and experiments is large, especially at current densities below 1 A/cm^2. This is again a possible effect of the natural convection of the gasses.

5.2. KOH concenctration

Increasing the KOH concentration in an electrolyzer decreases ohmic losses due to improved ionic conductivity. On the other hand, the KOH concentration also makes the liquid more viscous, thus increasing the pressure drop. Additionally, the solubility is drastically reduced with increasing KOH concentration, which could potentially decrease the bubble resistance onset concentration. This section will compare the base case to a case where the KOH concentration is 6M instead of 1M.

5.2.1. IV curves

The IV curves of the 1M and the 6M cases are shown in Fig. 5.6.

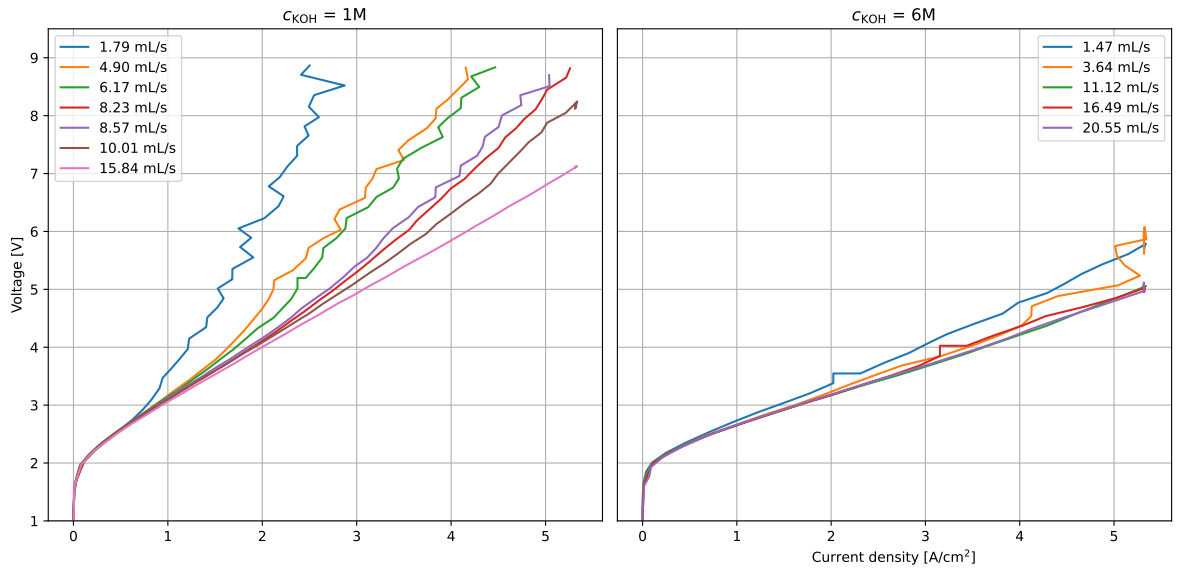

Figure 5.6: IV curves for 1M KOH and 6M KOH electrolyte, with a 0.8 mm interelectrode gap

The 6M case gives significantly lower overpotentials than the 1M case. This is caused by the 2.9 times higher conductivity of 6M KOH compared to 1M KOH. Interestingly, in the 6M case the resistance due to bubbles is substantially lower than in the 1M case. This is because of the high conductivity, which decreases the effect that bubbles have on resistance. This is especially interesting if flow-through electrolysis is used with low-conductive electrolytes, such as a brine stream. In these systems, the effect of bubble formation on resistance beyond the transition current may even be greater due to the low conductivity with respect to 1M KOH.

5.2.2. Pressure drop

The viscosity increases with the KOH concentration of the electrolyte [36]. Therefore, the pressure drop also increases with increasing molarity. The comparison between the pressure drop between the 1 molar and the 6 molar cases is shown in the figure below:

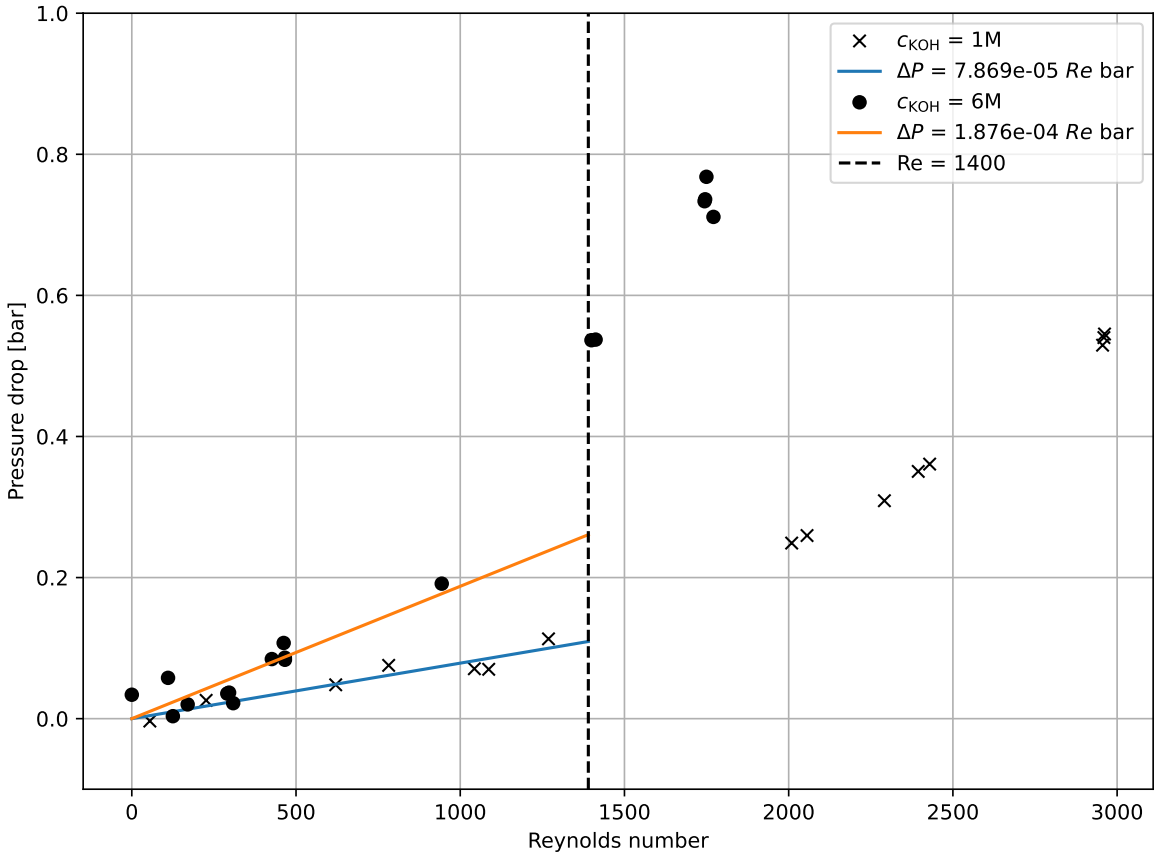

Figure 5.7: Pressure drop for 1M KOH and 6M KOH at various Reynolds numbers

Using Appendix A, it is found that the viscosity of the 6M electrolyte is about 1.8 times higher than that of the 1M electrolyte. From the theoretical pressure drop in Eq. (5.1), it is found that the pressure drop is proportional to the square of viscosity. This means that it is expected that the pressure drop is also around 3.2 times larger for the 6M case than for the 1M case. The fits in Fig (5.7) shows that the pressure drop of the 6M case is about 2.4 times higher than the 1M case. The difference can be explained by other losses dependent on the density or by the poor accuracy of the pressure sensor.

5.2.3. Power dissipation

Using Eq.(5.5) for the energy consumption per kg hydrogen and Eq. (5.6) for the HHV of hydrogen, the following graph can be made:

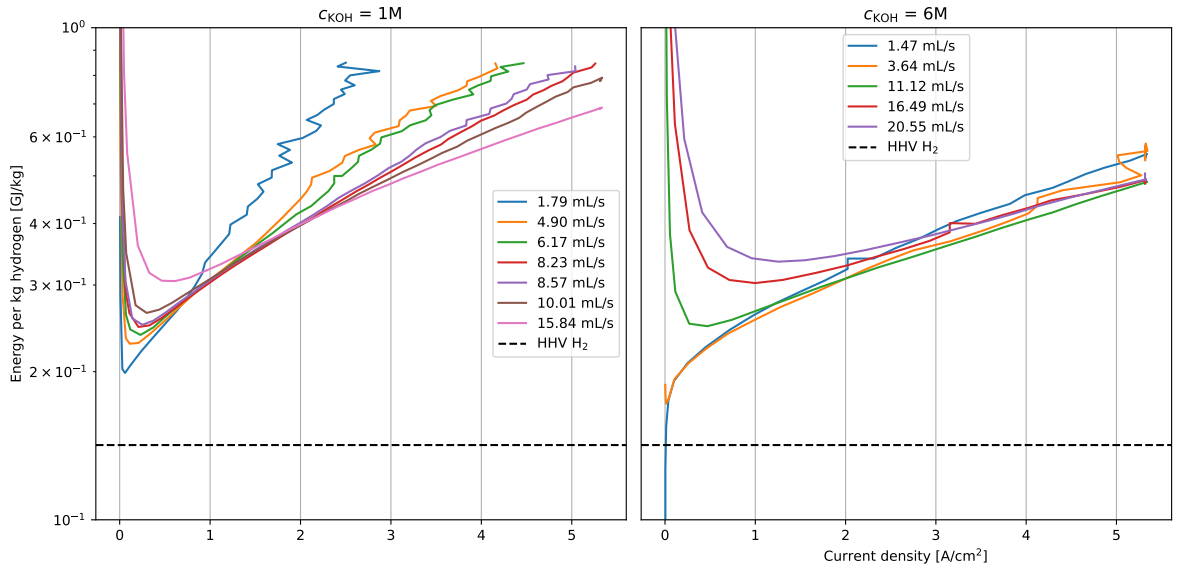

Figure 5.8: The energy per kg produced hydrogen using Eq. (5.5) for various flow rates for the two electrolyte concentrations

Because the difference in pressure drop between the 6M case and the 1M case is minimal, the 6M case outperforms the 1M case at every current density. Because the pressure drop stays constant with respect to the current density, the contribution of power dissipation due to pressure drop is increasingly small at higher current densities, as seen in Eq. (5.5). This makes that the 6M case always has a higher efficiency than the 1M case, regardless of its higher pressure drop.

5.2.4. Transition current density

In Fig. 5.9 the transition currents for the 2 different molar configurations are shown.

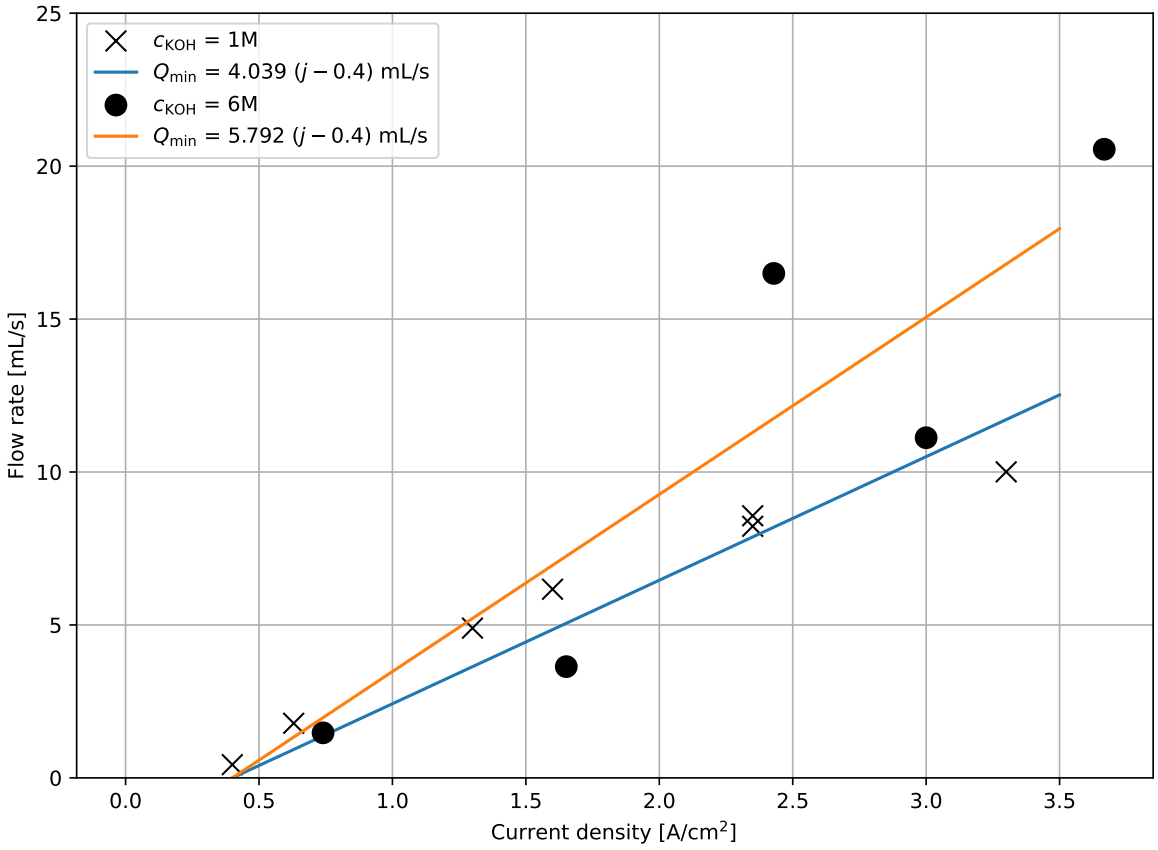

Figure 5.9: Transition current density, the current densities where the resistance due to bubbles starts to be noticeable, as a function of flow rate for the gaps. Each data set for a specific gap is followed by a curve fit where j is in A/cm^2

The higher concentration electrolyte shows a slightly higher necessary flow rate to avoid transitioning to the high resistance regime. This may be explained by the inferior solubility of 6M compared to 1M, which gives signs that the transition current density is dependent on the solubility, but not nearly as much as expected from Eq. (2.16). There needs to be dedicated research with more data points at different KOH concentrations to prove that the transition current density is dependent on the KOH concentration. However, this is beyond the scope of this research. The other possibility is that the KOH concentration does not have an effect on the transition current density. The data of the 6M test is more scattered with respect to the 1M case because it is harder to determine the transition current density due to the relatively small effect of the bubble resistances for the 6M case. Additionally, 3 of the 5 data points match the trend of the 1M case. In this case, a KOH concentration independent solubility can be constructed such that Eq. 5.8 fits the 1M fit. The solubility will be corrected to a value of 4.34 mol/m^3. This corrected solubility does not mean that hydrogen is actually dissolved in the electrolyte. It can be seen as the average concentration of hydrogen gas, both dissolved and in gaseous form, in the outlet flow and will be called the bubble resistance onset concentration.

5.2.5. corrected optimal KOH concentration

With the bubble resistance onset concentration of 4.34 mol/m^3 the theoretical relation of Eq. (2.37). If a low permeability is assumed ($k < 10^{-9}$ m^2) Eq. 2.38 can be used to show the effect of increasing the solubility on the optimal KOH concentration.

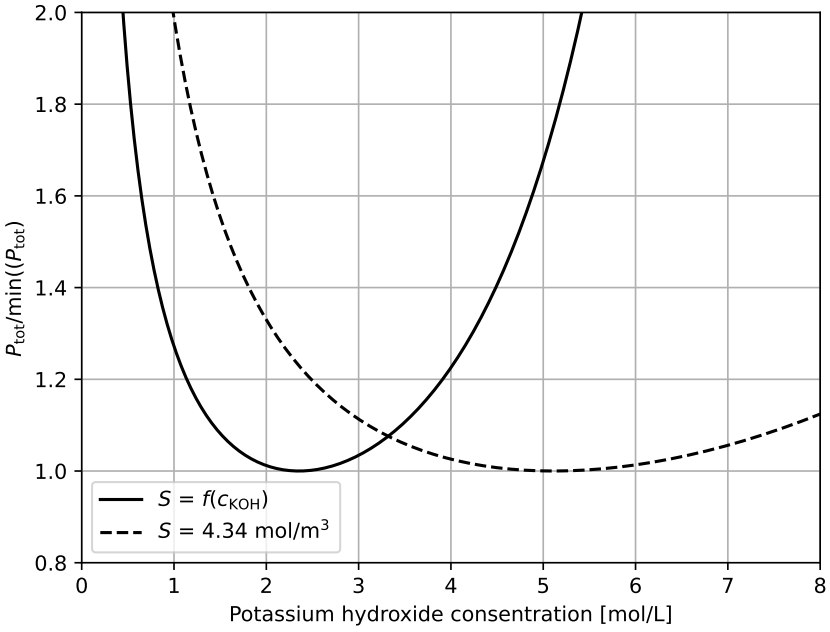

Figure 5.10: Plotting the analytical power dissipation as a function of the KOH concentration, using the KOH-dependent solubility from the works of Ruetschi et al. [37] and using the KOH-independent bubble onset concentration with a value of 4.34 mol/L as solubility

Using the bubble resistance onset concentration in Eq. (2.38), indeed shows that the optimum KOH concentration lies closer to the optimum KOH concentration of 6.1 M in conventional electrolyzers. To better validate the contribution of the KOH concentration to the total power dissipation in Eq. (2.38), more experiments at different KOH concentrations need to be run, but for now, it is a good indication that KOH concentrations close to 5M give higher efficiency.

5.3. Saturation effect

To further investigate the losses due to bubble formation, the electrolyte was degassed using a vacuum chamber. Subsequently, the electrolyte was inserted back into the system and IV sweeps were carried out. The IV sweeps were carried out at different time intervals to simulate the effect of the electrolyte getting more saturated with gasses. The results of the test are shown in Fig. 5.11

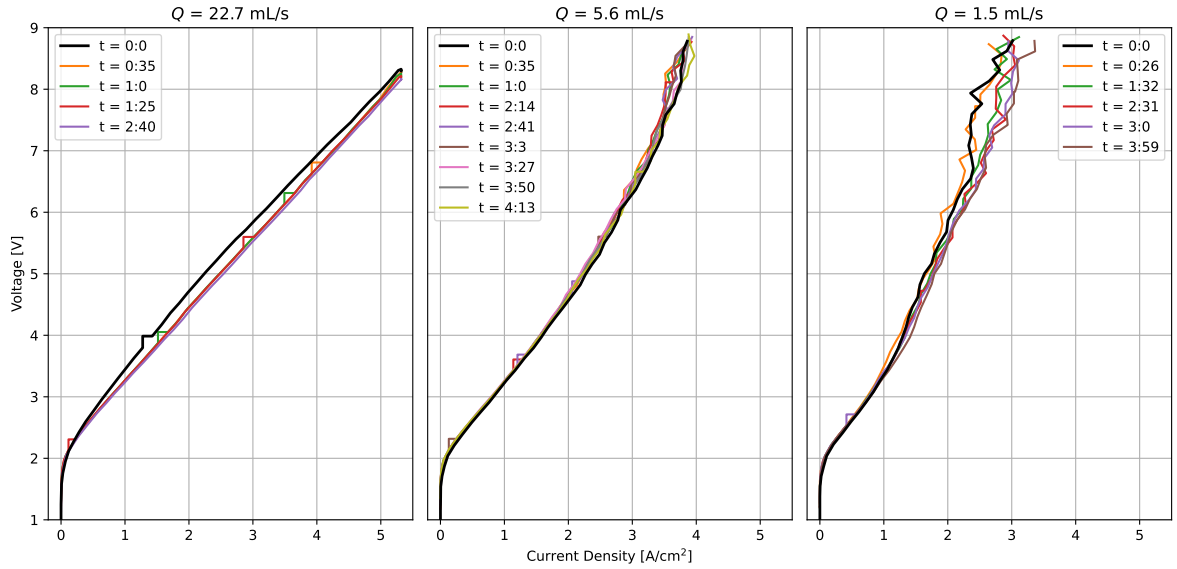

Figure 5.11: IV curves after degassing labelled with minutes : seconds after the first test

The IV curve of the experiment just after degassing denoted by the black line shows only slightly lower voltage at low current densities with respect to all the IV curves made after t = 0:0. A zoomed-in version of the low current regime is shown in the following figure:

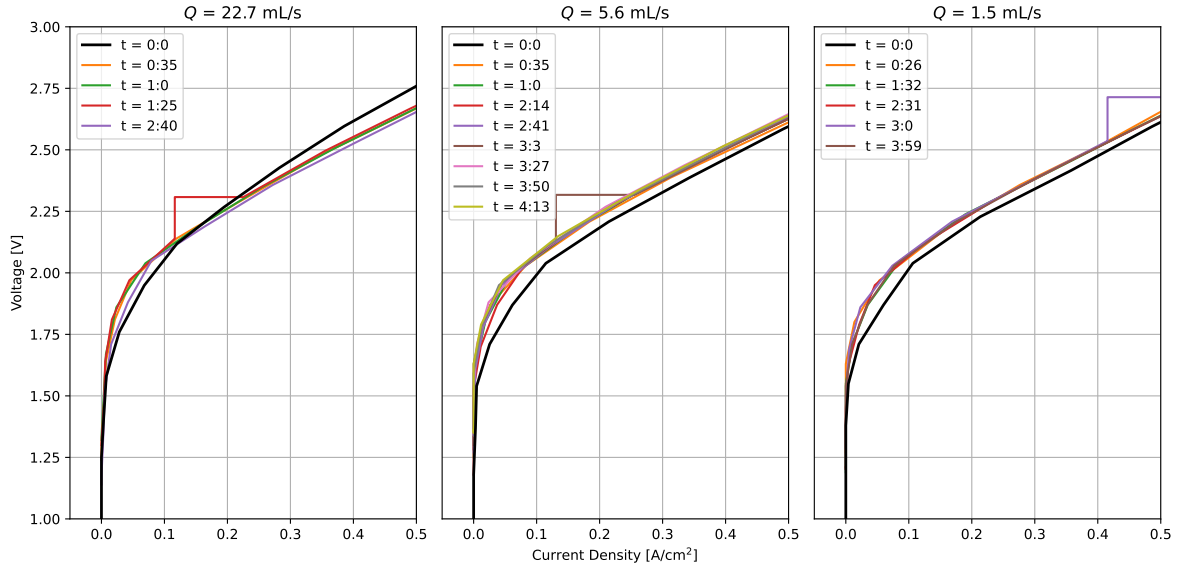

Figure 5.12: Zoomed in version of Fig. 5.11 at the lower current density regime with time steps labelled with minutes : seconds after the first test

A small reduction in overpotential is seen, which can be the effect of the reduced saturation of the electrolyte. For the degassing of the electrolyte, the electrolyzer needed to be drained. It is possible that due to the draining process, more electrode surface was freed from any leftover gas pockets after the operation. These pockets would reemerge after the first IV curve. This might also give the reduction in overpotential seen in Fig. 5.12. In spite of this effect, from now on the overpotential is assumed to be the cause of degassing the electrolyte. The 22.7 mL/s case shows a high overpotential current density above 0.1 A/cm^2. The nickel electrodes could have reacted when exposed to the air, creating nonconductive NiO pollution on the electrode surface [41]. The overpotential savings due to vacuum

degassing, $\delta\phi_{\text{vac}}$, will be expressed as the difference between the IV curve at t = 0:0 and the average of the IV curves after this timestep. The result is shown in Fig. 5.13.

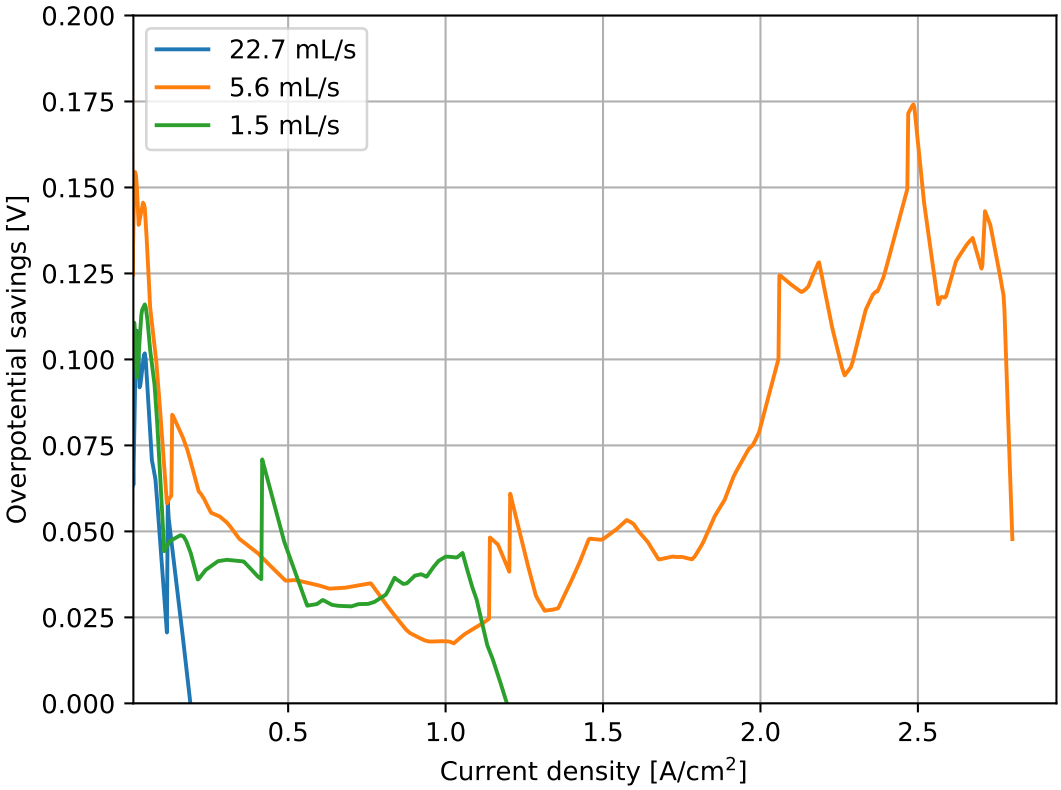

Figure 5.13: The overpotential savings by degassing, calculated by the difference in potential just after degassing and the average of the subsequential IV curves

The 5.6 mL/s case performs the best compared to the two other flow rates. Before 0.1 A/cm^2, the overpotential savings are quite similar. After 0.1 A/cm^2 the 22.7 mL/s case starts to deviate from the two other cases, with a very high overpotential, seen in Fig. 5.11. The 5.6 mL/s case seems to perform extra well at high current densities above 2 A/cm^2, which can be explained by the randomness of the IV curve after the transition current. For real energy savings, the energy used by degassing needs to be accounted for. If a perfect vacuum is assumed, the power used by degassing can be estimated by $P_{\text{vac}} = Q\Delta p = Qp_{\text{atm}}$. The energy savings can be expressed in the following form:

$$E_{\text{savings}} = \frac{FZ}{M_{\text{H}}}\left[\frac{Qp_{\text{atm}}}{jA} + \Delta\phi_{\text{vac}}\right] \tag{5.9}$$

From this equation, the estimated energy savings can be plotted as a function of current density. Because the energy savings are mostly negative, the next figure will express the energy losses as a function of current density:

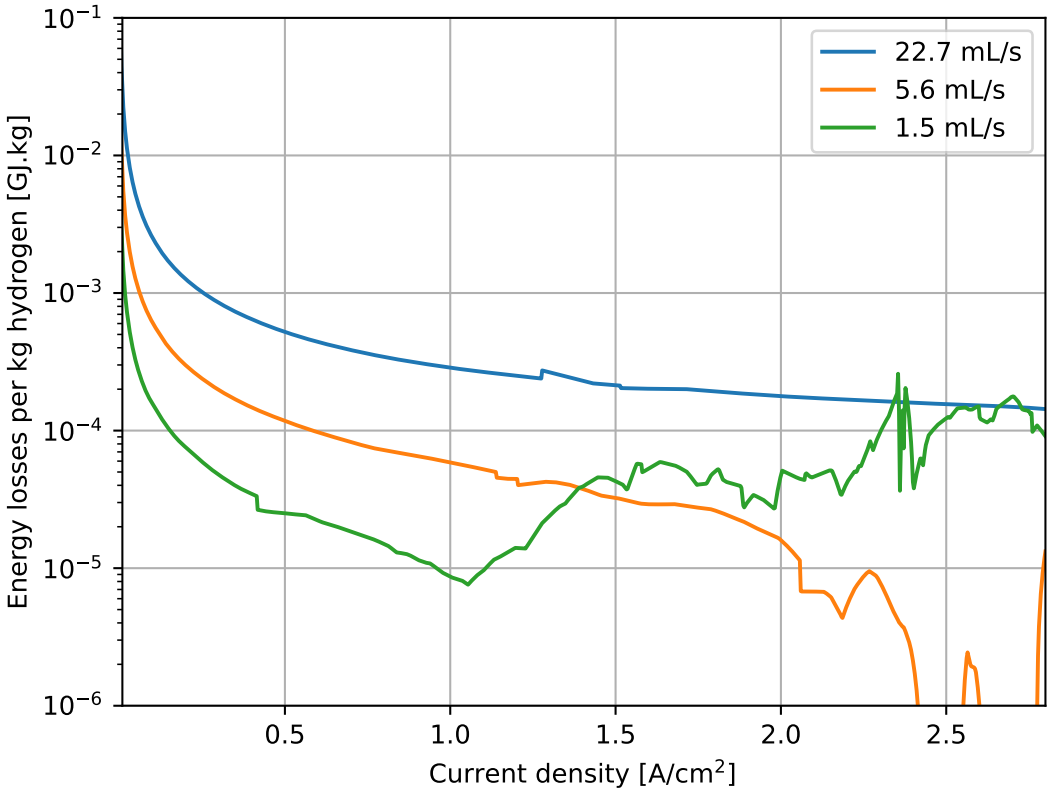

Figure 5.14: The energy losses due to vacuum degassing expressed in GJ per kg hydrogen as a function of the current density

Except for a small regime in the 5.6 mL/s case, the vacuum degassing negatively affected the efficiency of the electrolyzer. The case that degassing did save energy, was after the transition current, which means the overall efficiency is low due to bubble losses. Besides requiring more energy than saving, the degassing step adds extra complexity to the system which makes the electrolyzer more costly.

In another test, the back of the cathode was recorded using the microscope camera. In this case, the interelectrode gap was 1.5 mm, because this test had the clearest images. In this experiment, three snapshots are given at different current densities with three different flow rates:

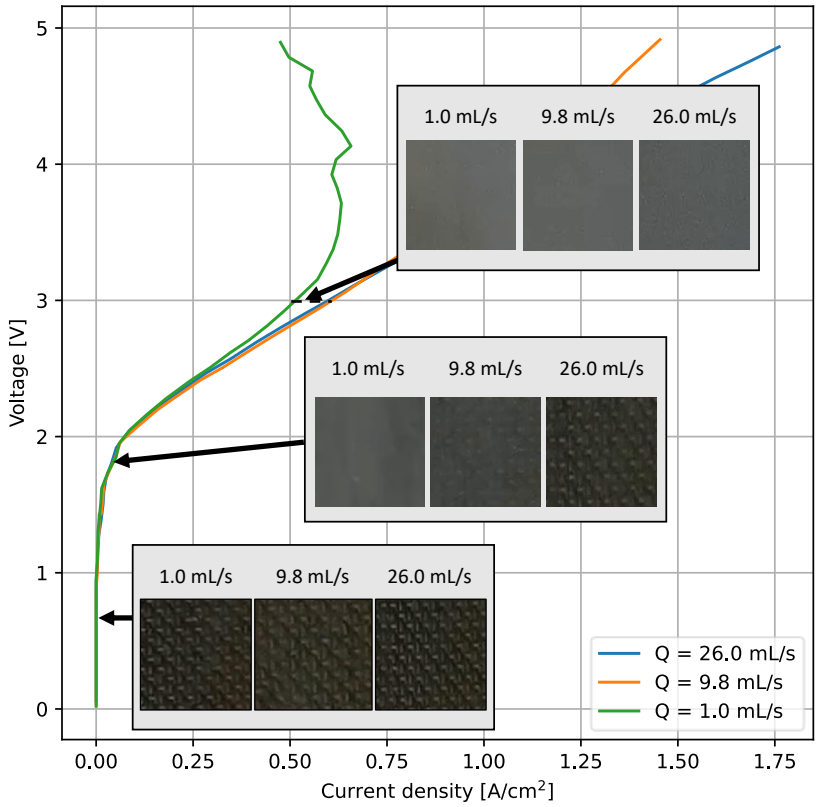

Figure 5.15: IV curves of the electrolyzer with a 1.5 mm interelectrode gap with snapshots taken perpendicular from the back at the cathode at specific current densities

The image at 1.8 Volts shows that in the 26 mL/s case, the gas is mostly saturated in the electrolyte. In this image, there are no bubbles visible. The 9.8 mL/s case already shows many more bubbles that create a haze in front of the electrode, and in the 1.0 mL/s case, the electrode is barely visible. The IV curves nearly overlap, which further shows that the effect of keeping the gasses saturated has only a small effect on the overpotential.

5.4. Variable discharge channel

In this research, a discharge channel geometry was designed to make the flow across the electrodes more uniform. In this next section, this variable discharge geometry is tested in experiments and compared to a straight channel geometry.

5.4.1. IV curves

As usual, the IV curves are first shown to understand the electrical performance of the two discharge channel shapes.

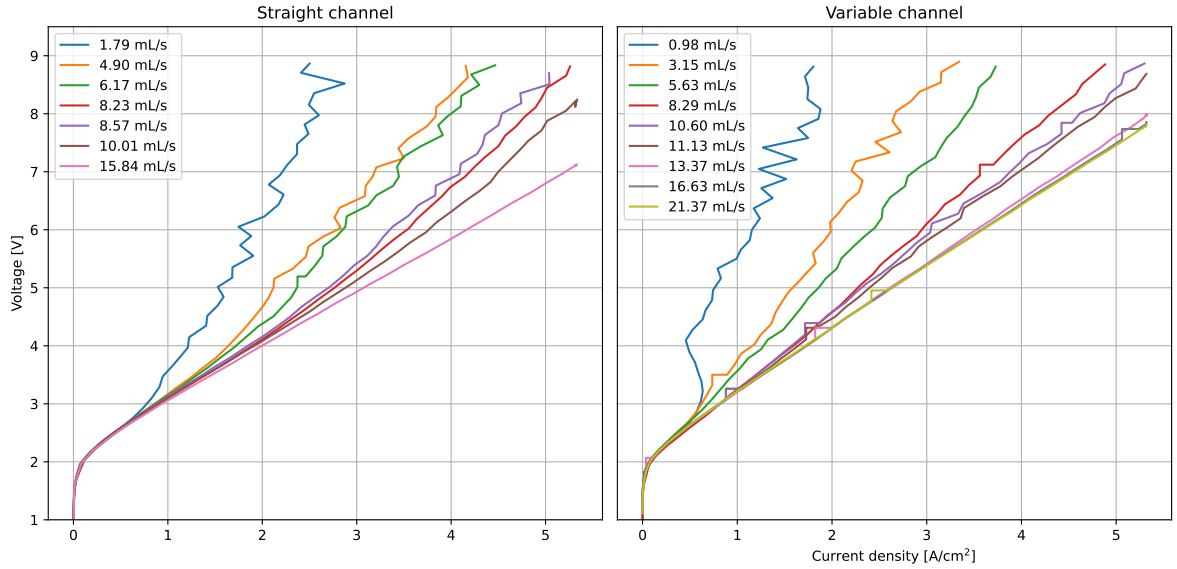

Figure 5.16: IV curves for the straight and variable discharge channel geometry

Interestingly, the variable discharge channel case has a higher ohmic resistance than the straight discharge channel case. There is insufficient data to explain why this difference occurs. A hypothesis could be that the variable discharge channel is designed to optimize a flow with dissolved gasses, and therefore might have different performance when there is bubble formation.

5.4.2. Pressure drop

In Fig. 5.17 the pressure drop in the variable discharge channel gives a higher pressure drop than the straight discharge channel.

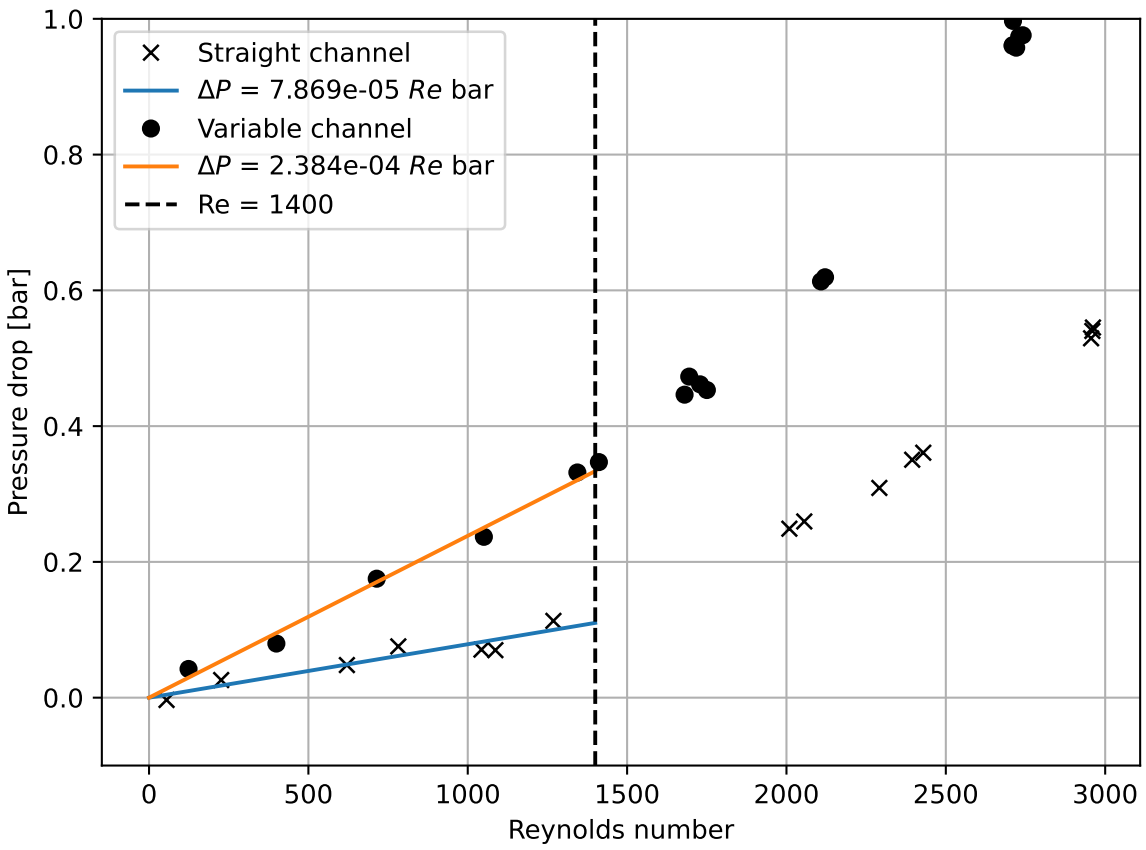

Figure 5.17: Pressure drop for the straight and variable discharge channel geometry at various Reynolds numbers

This is not expected as the CFD simulations gave a lower pressure drop for the variable discharge channel case. This is possible because of the poor resolution of the pressure sensor.

5.4.3. Power dissipation

The energy needed to produce one kilogram of hydrogen for both geometries is shown in Fig. 5.18.

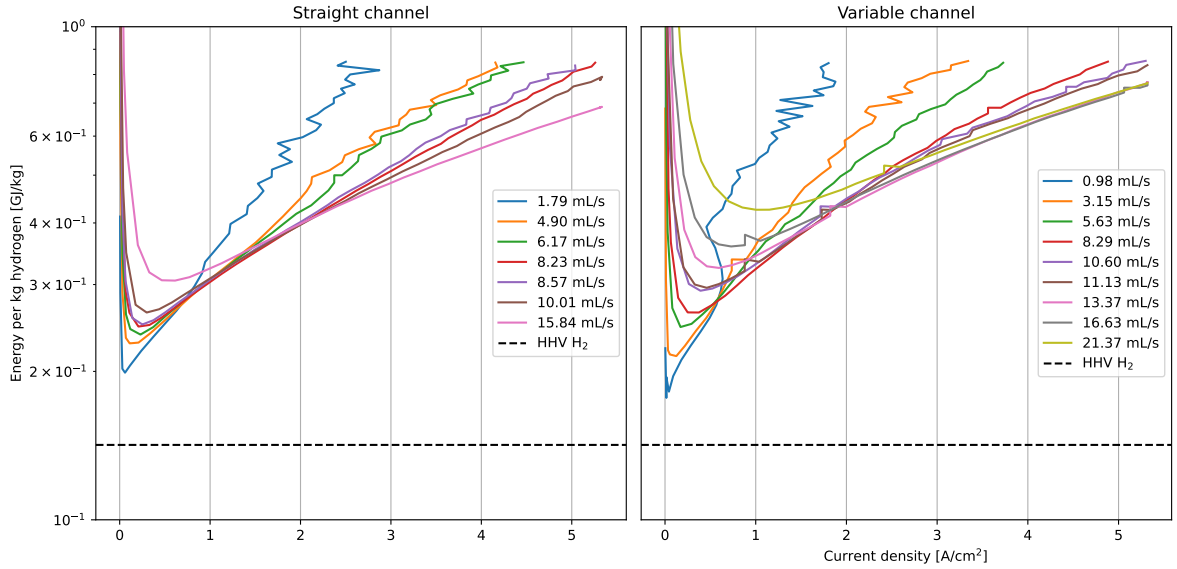

Figure 5.18: Total power dissipation for the straight and variable discharge channel geometry

The pressure drop and the overpotential were both higher in the variable discharge channel case than in the straight discharge channel case. This gives the variable discharge channel a lower efficiency. Meanwhile, the complexity of such a discharge channel is far greater than that of a straight discharge channel, which would give an increase in capital cost.

5.4.4. Transition current density

Besides the worse efficiency of the variable discharge channel, the transition current densities also have lower values, meaning the necessity of a higher flow rate to prevent resistance due to bubbles. This can be seen in Fig. 5.19.

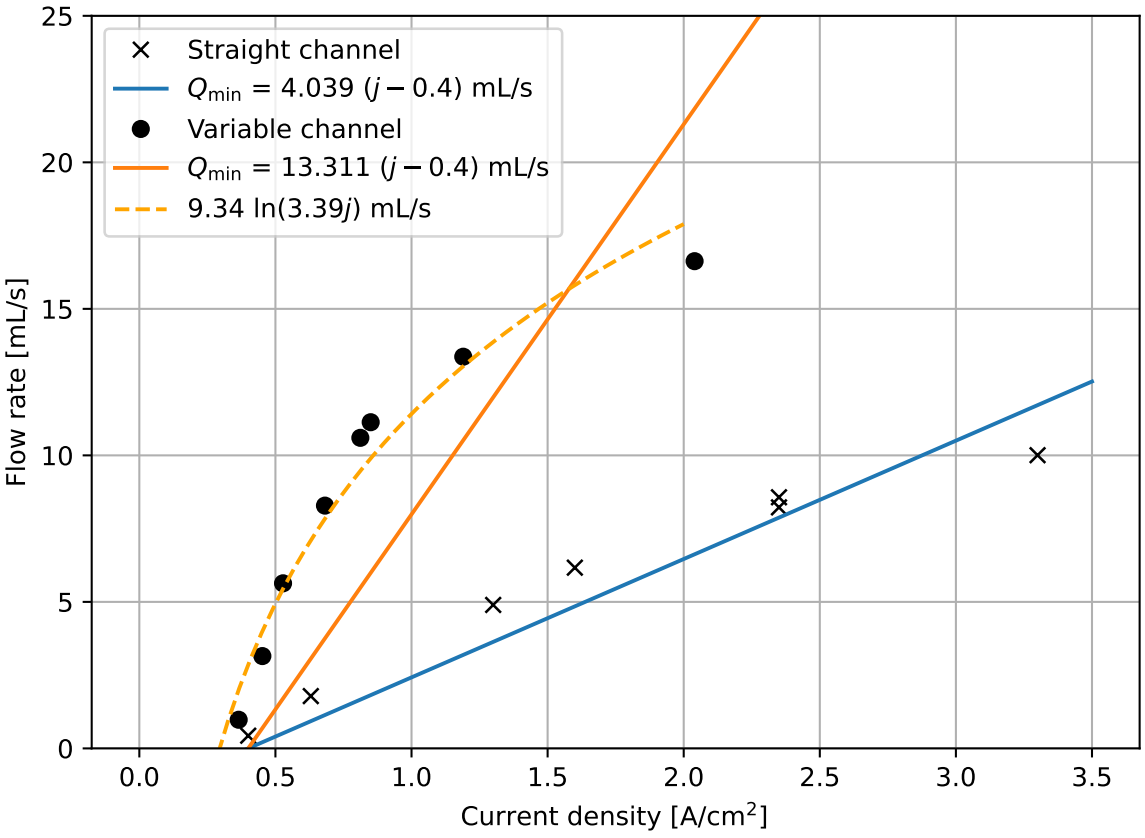

Figure 5.19: Minimum flow rate necessary before transitioning to higher resistance for the straight discharge channel case and the variable discharge channel case. An extra logarithmic fit is added to the variable discharge channel case to illustrate the nonlinear behaviour of the transition current density

Again, because of the lack of data, the difference in performance can not be explained. As said before, the transition current densities show a nonlinear relation to the flow rate, which is especially prominent in the variable discharge channel case. To illustrate this, a logarithmic fit is added to the data for the variable discharge channel case.

6

Conclusion

In this report, a flow-through electrolyzer was optimized to reduce resistances in the electrolyte due to bubble formation. In the introduction, the research questions were made which will be answered below to draw a conclusion.

What effect on efficiency does keeping hydrogen and oxygen gas dissolved in the electrolyte have on a flow-through alkaline water electrolyzer?
Using the results of the degassing experiment in Fig. 5.11, Fig. 5.12, and Fig. 5.13, it was found that the effect of degassing saves around 50-150 mV overpotential at current densities below 1 A/cm^2. This was either because the electrolyte was decreased in gas saturation or the removal of gas pockets due to the requirement of draining the electrolyzer before degassing. The latter would mean that the effect on the overpotential of degassing is negligible with respect to the other losses in the system. In both cases, the energy required to degas the electrolyte exceeded the saved energy by reducing the overpotential, seen in Fig. 5.14, and therefore harms the efficiency of the electrolyzer. It might be possible to make an efficient electrolyzer if the flow is minimal to negate the power dissipation due to pressure losses. While the flow rate is proportional to the transition current density, the current density should be chosen below the described fits in Fig. 5.9 to avoid losses due to the bubble resistance. In contrast, in Fig. 5.14 the saved power due to degassing increases with current density. This would make the net power savings very low, or even negative for low current densities (< 1A/cm^2). Another possibility instead of using a vacuum chamber, is to pressurize the system to negate the effect due to bubble formation. Such a system is explained in the recommendations. For now, it can be concluded that in the current setup at current densities below 1A/cm^2, keeping the gasses dissolved has a negative impact on the efficiency of the electrolyzer.

What flow rate is needed to keep the losses in an electrolyzer due to bubble formation and pressure drop at a minimum?
In the theory chapter, it was hypothesized that the solubility of hydrogen governed the flow rate. With this hypothesis Eq. (2.16) was constructed. However, the results showed that changing the solubility was not directly related to the solubility. Figure 5.9 shows that changing the KOH concentration has a small effect on the needed flow rate in order to prevent resistance due to bubble formation. This flow rate was 1.5 times higher for the 1M electrolyte case with respect to the 6M electrolyte case, while the solubility is 4.5 times higher. This could effectively mean two things, the possibility of supersaturating the gasses in the electrolyte or the resistance due to gasses being only measurable at a certain amount of gas production. Instead of using the solubility as a measure of the necessary flow rate, the bubble resistance onset concentration was introduced, with a value of 4.34 mol/m^3 for 1M electrolyte. Another hypothesis that played a role in the required flow rate to negate losses due to bubbles is the wall shear rate. It was found that for the three feed channel sizes in Fig. 5.4 the resistance due to bubbles happened at different current densities. Because changing feed channel size should not affect the flow passing the electrodes, the difference in the current density where any noticeable bubble resistance could be the cause of the shear rate at the electrodes inside the feed channel. This gives an indication of the flow velocity close to the electrodes, which is linked to the rate of bubbles leaving the electrode

surface. Table 5.3 shows that there might be a relation between wall shear rate and the current density where the bubbles begin to take an effect on the resistance. In conclusion, the flow rate needed to prevent bubble resistance depends on the current density and the size of the feed channel. The solubility of hydrogen in electrolytes seems to have a small effect on this resistance.

What shape does the discharge channel need to be to distribute the flow uniformly across the electrodes, to ensure saturation across the electrode of product gasses and to keep the pressure drop across the electrodes at a minimum?
Using the analytically obtained relation in Eq. (2.14), the shape of the discharge channel was determined to promote a uniform flow across the electrodes. The channel was numerically analysed in Comsol. An Euler number was higher than 10, the variable discharge channel gave better uniformity than a conventional straight discharge channel. At low permeabilities and inlet velocities, the variable discharge channel geometry could even approach a uniform flow, whereas the straight channel would never get a uniform flow across the electrodes. From the results, the variable discharge channel had a worse performance both on pressure drop and the bubble resistance than expected from theory and simulations. On top of this, the transition current densities are lower for specific flow rates than using a straight outlet channel. The results were inconclusive on why the difference between the two cases is big.

What is the optimum potassium hydroxide concentration for running the electrolyzer?
The power dissipation is dependent on viscosity, solubility and ionic conductivity. All these variables have a dependency on the KOH concentration, shown in Appendix A. From the theoretical equation, Eq. (2.37), it was expected that solubility plays a big role in the optimum KOH concentration. However, from experiments, it was observed keeping the gasses dissolved did not significantly improve the efficiency of the electrolyzer. This means that the dependency on solubility was less than expected. After correcting the solubility to a value of 4.34 mol/m^3, the optimum KOH concentration was around 4 to 6 molars.

General Conclusion
The main research question from this thesis is:

What geometry and fluid variables achieve the lowest power dissipation at atmospheric conditions in an alkaline flow-through water electrolyzer in order to minimize the losses due to bubble formation?

The minimum power dissipation in a flow-through electrolyzer depends on the application of the electrolyzer plant. Electrolyzers need to run at high current densities to reduce the necessary electrode area and therefore the capital cost of an electrolyzer plant. For a high current density, you need a high flow rate to remove the produced gasses before they start interfering with the ion flux between the electrodes and increasing the resistance in the electrolyte. The inter-electrode gap should be small decrease ohmic resistance between the electrodes and possibly promotes the departure of bubbles on the electrode surface, which both have a positive effect on the efficiency. If the operational costs outweigh the capital cost, a high-efficiency electrolyzer is beneficial. High efficiency is reached at low current density, due to the reduced effects of ohmic power losses. The flow should also be minimal, to keep the power dissipation due to the pressure drop at a minimum. The solubility of the electrolyte does not play a big role in the total power dissipation, therefore a high concentration electrolyte around 5M is needed for the highest efficiency, even if this high concentration of KOH drastically lowers the solubility. Furthermore, the shear rate is potentially an important factor in the design of the electrolyzer as it induces bubble removal from the electrode surface. Keeping the gasses dissolved potentially gives a slight decrease in resistance but in this setup, is outweighed by the added complexity and pumping losses.

7

Recommendation

7.1. High-temperature flow-through electrolysis

In this research, the system was kept under atmospheric conditions for simplicity. To further improve the efficiency of the electrolyzer, the electrolyte can be heated up to increase the conductivity of the electrolyte [27]. A flow-through electrolyzer would be an excellent choice because it does not have a membrane which degrades when exposed to high temperatures and allows temperatures beyond 100 $^{\circ}$C.

7.2. High-pressure flow-through electrolysis

In this thesis, it was also concluded that keeping gasses saturated reduces the overpotential, but is not viable due to the losses of the high necessary flow rate. Increasing the pressure might be a solution to this problem because the solubility of hydrogen is heavily dependent on the pressure of the electrolyte. From the research of Wiebe et al. [28], it is shown that hydrogen solubility increases linearly with pressure. Operating under high pressure in the electrolyzer, it is possible to keep the gasses saturated without the need for a very high flow rate. Extraction of the dissolved hydrogen is also much simpler because the product stream can be depressurized to nucleate the hydrogen and later be separated from the electrolyte in a gas-liquid separator. An example process is shown in fig. 7.1

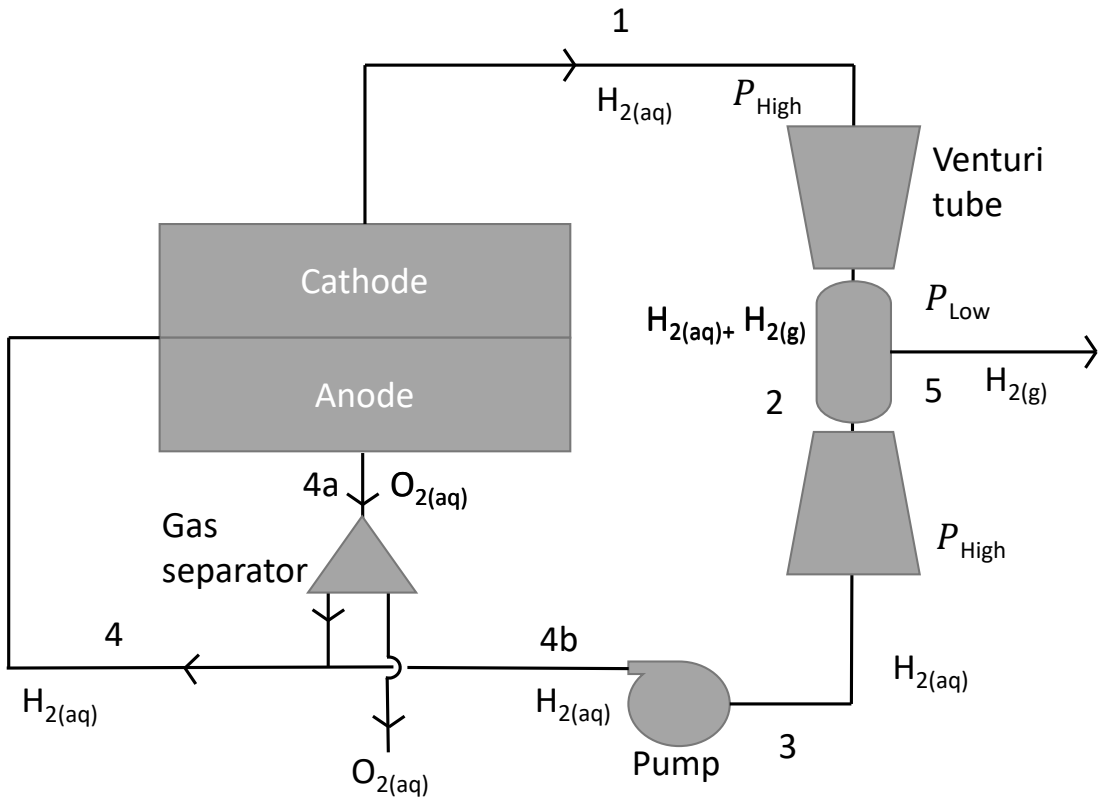

Figure 7.1: Example process using pressure to remove hydrogen from the electrolyte. The Venturi tube accelerates the high-pressure dissolved hydrogen product stream '1', leading to the low-pressure stream '2'. Due to the pressure drop, the hydrogen nucleates into gas, which can be separated into stream '5' as the hydrogen gas outlet, and stream '3' as a degassed electrolyte with a small amount of leftover hydrogen which is recycled in the system. Stream '3' is pressurized due to the deceleration of the stream at the outlet of the venturi tube. Using the pump, an additional head is applied to the flow to overcome the losses. Stream '4a' is the anode product stream with dissolved oxygen. This gas separated from the product stream. An example of such a technique is using nitrogen gas to strip the dissolved oxygen from the electrolyte. Stream '4a' and '4b' are then combined into stream '4', which is used as an inlet for the electrolyzer.

In this example, the liquid stream is degassed with a Venturi tube. The product stream, '1', is accelerated by decreasing the pipe diameter, causing a drop in pressure due to Bernoulli's principle:

$$\Delta P = -\frac{1}{2}\rho\Delta(V^2) \tag{7.1}$$

Using mass conservation (${V_1}{D_1}^2 = {V_2}{D_2}^2$) Eq. 7.2 can be changed to the following form:

$$P_2 - P_1 = -\frac{1}{2}\rho {V_1}^2 \left(\left[\frac{D_1}{D_2}\right]^4 - 1\right) \tag{7.2}$$

As said before, the solubility will drop linearly with the pressure drop. Assuming product stream 1 is saturated with hydrogen, the following relation can be made:

$$\frac{P_{\text{Low}}}{P_{\text{High}}} = \frac{S_2}{S_1} = \frac{[\text{H}_{2(\text{aq})}]_2}{[\text{H}_{2(\text{aq})}]_1} \tag{7.3}$$

From this, it is possible to determine the hydrogen product stream:

$$[\text{H}_{2(\text{g})}]_5 = [\text{H}_{2(\text{aq})}]_1 - [\text{H}_{2(\text{aq})}]_2 = [\text{H}_{2(\text{aq})}]_1 \left(1 - \frac{P_2}{P_1}\right) \tag{7.4}$$

The same relation can also be expressed in the ratio of pipe diameters by combining Eq. 7.3 and Eq. 7.4:

$$[\mathrm{H_{2(g)}}]_5 = [\mathrm{H_{2(aq)}}]_1 \frac{\rho {V_1}^2}{2P_1} \left(\left[\frac{D_1}{D_2} \right]^4 - 1 \right) \tag{7.5}$$

7.2.1. Bubble shear and supersaturation

From the results of this research, it was found that the transition in resistance was possibly governed by bubble formation or had something to do with supersaturation. In this study, it was not possible to look between the two electrodes, due to the small gap in between. Using a high-speed camera with a view between the two electrodes would be great for understanding the bubble dynamics in alkaline flow-through electrolysis especially, to see what exactly is happening near the electrodes inside the feed channel. The gap does not have to be small, as the dynamics are more interesting in this case than obtaining the highest electrolyzer efficiency. Besides the specific case of a flow-through electrolyzer, it would also be interesting to see what exactly happens with bubble dynamics near the electrodes at the transition current densities. This can maybe explain supersaturation near the electrodes and help better optimize the design for a flow-through electrolyzer.

References

[1] S. A. Sherif, Frano Barbir, and T. N. Veziroglu. “Towards a Hydrogen Economy”. In: *The Electricity Journal* 18.6 (July 2005), pp. 62–76. ISSN: 1040-6190. DOI: 10.1016/J.TEJ.2005.06.003.

[2] Wenguo Liu et al. *The production and application of hydrogen in steel industry*. 2021. DOI: 10.1016/j.ijhydene.2020.12.123.

[3] Nigel Rambhujun et al. *Renewable hydrogen for the chemical industry*. 2020. DOI: 10.1557/mre.2020.33.

[4] IRENA - International Renewable Energy Agency. *Hydrogen*. 2022. URL: https://www.irena.org/Energy-Transition/Technology/Hydrogen#:~:text=As%20at%20the%20end%20of,around%204%25%20comes%20from%20electrolysis..

[5] Jörn Brauns and Thomas Turek. *Alkaline water electrolysis powered by renewable energy: A review*. 2020. DOI: 10.3390/pr8020248.

[6] Md Mamoon Rashid et al. “Hydrogen Production by Water Electrolysis: A Review of Alkaline Water Electrolysis, PEM Water Electrolysis and High Temperature Water Electrolysis”. In: *International Journal of Engineering and Advanced Technology* 3 (2015).

[7] Daniel V. Esposito. “Membraneless Electrolyzers for Low-Cost Hydrogen Production in a Renewable Energy Future”. In: *Joule* 1.4 (Dec. 2017), pp. 651–658. ISSN: 2542-4351. DOI: 10.1016/J.JOULE.2017.07.003.

[8] Alessandro Manzotti, Matthew J. Robson, and Francesco Ciucci. “Recent developments in membraneless electrolysis”. In: *Current Opinion in Green and Sustainable Chemistry* 40 (Apr. 2023), p. 100765. ISSN: 2452-2236. DOI: 10.1016/J.COGSC.2023.100765. URL: https://linkinghub.elsevier.com/retrieve/pii/S2452223623000147.

[9] Isaac Holmes-Gentle et al. “Membrane-less photoelectrochemical cells: Product separation by hydrodynamic control”. In: *Sustainable Energy and Fuels* 1.5 (2017). ISSN: 23984902. DOI: 10.1039/c7se00176b.

[10] G. Segré and A. Silberberg. “Radial particle displacements in poiseuille flow of suspensions”. In: *Nature* 189.4760 (1961). ISSN: 00280836. DOI: 10.1038/189209a0.

[11] S. Mohammad H. Hashemi, Miguel A. Modestino, and Demetri Psaltis. “A membrane-less electrolyzer for hydrogen production across the pH scale”. In: *Energy and Environmental Science* 8.7 (July 2015), pp. 2003–2009. ISSN: 17545706. DOI: 10.1039/c5ee00083a.

[12] S. Mohammad H. Hashemi et al. “A versatile and membrane-less electrochemical reactor for the electrolysis of water and brine”. In: *Energy and Environmental Science* 12.5 (2019). ISSN: 17545706. DOI: 10.1039/c9ee00219g.

[13] Biswajit S. De et al. “An electrochemical neutralization energy-assisted membrane-less microfluidic reactor for water electrolysis”. In: *Sustainable Energy and Fuels* 4.12 (2020). ISSN: 23984902. DOI: 10.1039/d0se01474e.

[14] Xueqi Pang et al. “Framework for evaluating the performance limits of membraneless electrolyzers”. In: *Energy and Environmental Science* 13.10 (Oct. 2020), pp. 3663–3678. ISSN: 17545706. DOI: 10.1039/d0ee02268c.

[15] Feichen Yang et al. “Alkaline Water Electrolysis at 25 A cm−2 with a Microfibrous Flow-through Electrode”. In: *Advanced Energy Materials* 10.25 (2020). ISSN: 16146840. DOI: 10.1002/aenm.202001174.

[16] James A. Trainham and John Newman. “A comparison between flow-through and flow-by porous electrodes for redox energy storage”. In: *Electrochimica Acta* 26.4 (Apr. 1981), pp. 455–469. ISSN: 0013-4686. DOI: 10.1016/0013-4686(81)87024-7.

[17] Peter S. Fedkiw. “Ohmic Potential Drop in Flow□Through and Flow□By Porous Electrodes”. In: *Journal of The Electrochemical Society* 128.4 (1981). ISSN: 0013-4651. DOI: 10.1149/1.2127513.

[18] M. Paulin, D. Hutin, and F. Coeuret. “Theoretical and Experimental Study of Flow□Through Porous Electrodes”. In: *Journal of The Electrochemical Society* 124.2 (1977). ISSN: 0013-4651. DOI: 10.1149/1.2133262.

[19] Roman E. Sioda et al. “FLOWTHROUGH POROUS ELECTRODES.” In: *Chemical Engineering (New York)* 90.4 (1983). ISSN: 00092460. DOI: 10.1149/1.2134076.

[20] Tim Risch and John Newman. “A Theoretical Comparison of Flow□Through and Flow□By Porous Electrodes at the Limiting Current”. In: *Journal of The Electrochemical Society* 131.11 (1984). ISSN: 0013-4651. DOI: 10.1149/1.2115357.

[21] M. I. Gillespie, F. Van Der Merwe, and R. J. Kriek. “Performance evaluation of a membraneless divergent electrode-flow-through (DEFT) alkaline electrolyser based on optimisation of electrolytic flow and electrode gap”. In: *Journal of Power Sources* 293 (2015). ISSN: 03787753. DOI: 10.1016/j.jpowsour.2015.05.077.

[22] M. I. Gillespie and R. J. Kriek. “Scalable hydrogen production from a mono-circular filter press Divergent Electrode-Flow-Through alkaline electrolysis stack”. In: *Journal of Power Sources* 397 (Sept. 2018), pp. 204–213. ISSN: 0378-7753. DOI: 10.1016/J.JPOWSOUR.2018.07.026.

[23] Glen D. O’Neil et al. “Hydrogen Production with a Simple and Scalable Membraneless Electrolyzer”. In: *Journal of The Electrochemical Society* 163.11 (2016), F3012–F3019. ISSN: 0013-4651. DOI: 10.1149/2.0021611jes.

[24] H. Rajaei, A. Rajora, and J. W. Haverkort. “Design of membraneless gas-evolving flow-through porous electrodes”. In: *Journal of Power Sources* 491 (Apr. 2021). ISSN: 03787753. DOI: 10.1016/j.jpowsour.2020.229364.

[25] Kai Zeng and Dongke Zhang. *Recent progress in alkaline water electrolysis for hydrogen production and applications*. June 2010. DOI: 10.1016/j.pecs.2009.11.002.

[26] Stefania Marini et al. “Advanced alkaline water electrolysis”. In: *Electrochimica Acta* 82 (2012). ISSN: 00134686. DOI: 10.1016/j.electacta.2012.05.011.

[27] R. J. Gilliam et al. “A review of specific conductivities of potassium hydroxide solutions for various concentrations and temperatures”. In: *International Journal of Hydrogen Energy* 32.3 (2007). ISSN: 03603199. DOI: 10.1016/j.ijhydene.2006.10.062.

[28] R. Wiebe and V. L. Gaddy. “The Solubility of Hydrogen in Water at 0, 50, 75 and 100° from 25 to 1000 Atmospheres”. In: *Journal of the American Chemical Society* 56.1 (1934). ISSN: 15205126. DOI: 10.1021/ja01316a022.

[29] H. Janssen et al. “Safety-related studies on hydrogen production in high-pressure electrolysers”. In: *International Journal of Hydrogen Energy* 29.7 (2004). ISSN: 03603199. DOI: 10.1016/j.ijhydene.2003.08.014.

[30] Emmanuel Zoulias and Elli Varkaraki. “A review on water electrolysis”. In: *Tcjst* 4.2 (2004).

[31] Diogo M. F. Santos, César A. C. Sequeira, and José L. Figueiredo. “Hydrogen production by alkaline water electrolysis”. In: *Química Nova* 36.8 (2013), pp. 1176–1193. ISSN: 0100-4042. DOI: 10.1590/S0100-40422013000800017. URL: http://www.scielo.br/scielo.php?script=sci_arttext&pid=S0100-40422013000800017&lng=en&nrm=iso&tlng=en.

[32] W. Wang et al. “Electrochemical cells for medium-and large-scale energy storage: Fundamentals”. In: *Advances in Batteries for Medium and Large-Scale Energy Storage: Types and Applications*. 2015. DOI: 10.1016/B978-1-78242-013-2.00001-7.

[33] Kai Zeng and Dongke Zhang. *Recent progress in alkaline water electrolysis for hydrogen production and applications*. June 2010. DOI: 10.1016/j.pecs.2009.11.002.

[34] Shigeo Shibata. “The Anodic Behavior of Cathodically Prepolarized Bright Platinum Electrode in Sulfuric Acid Solution”. In: *Bulletin of the Chemical Society of Japan* 33.12 (1960). ISSN: 0009-2673. DOI: 10.1246/bcsj.33.1635.

[35] Hisayoshi Matsushima, Daisuke Kiuchi, and Yasuhiro Fukunaka. “Measurement of dissolved hydrogen supersaturation during water electrolysis in a magnetic field”. In: *Electrochimica Acta* 54.24 (Oct. 2009), pp. 5858–5862. ISSN: 00134686. DOI: 10.1016/j.electacta.2009.05.044.

[36] K. I. Kuznetsov, S. V. Skorodumov, and P. P. Granchenko. “Measurements of the Dynamic Viscosity and Density of KOH Solutions at Atmospheric Pressure”. In: *High Temperature* 58.6 (2020). ISSN: 16083156. DOI: 10.1134/S0018151X20060127.

[37] P. Ruetschi and R. F. Amlie. “Solubility of hydrogen in potassium hydroxide and sulfuric acid. Salting-out and hydration”. In: *Journal of Physical Chemistry* 70.3 (1966). ISSN: 00223654. DOI: 10.1021/j100875a018.

[38] G. A. Whan and R. R. Rothfus. “Characteristics of transition flow between parallel plates”. In: *AIChE Journal* 5.2 (1959). ISSN: 15475905. DOI: 10.1002/aic.690050215.

[39] Yoshiyuki Asakura and Keiji Yasuda. “Frequency and power dependence of ultrasonic degassing”. In: *Ultrasonics Sonochemistry* 82 (Jan. 2022), p. 105890. ISSN: 1350-4177. DOI: 10.1016/J.ULTSONCH.2021.105890.

[40] NIST. *Isobaric Properties for Hydrogen*. 2021. URL: https://webbook.nist.gov/cgi/fluid.cgi?P=0.1+MPa&TLow=0&THigh=20&TInc=5&Digits=5&ID=C1333740&Action=Load&Type=IsoBar&TUnit=C&PUnit=MPa&DUnit=mol%2Fl&HUnit=kJ%2Fmol&WUnit=m%2Fs&VisUnit=uPa*s&STUnit=N%2Fm&RefState=DEF.

[41] S. L. Medway et al. “In situ studies of the oxidation of nickel electrodes in alkaline solution”. In: *Journal of Electroanalytical Chemistry* 587.1 (Feb. 2006), pp. 172–181. ISSN: 1572-6657. DOI: 10.1016/J.JELECHEM.2005.11.013.

A

Appendix

The ionic conductivity, κ, viscosity, μ, the density, ρ, and the solubility of hydrogen in water, S, all depend on the potassium hydroxide concentration and the temperature of the water.

Ionic conductivity

For the ionic conductivity, Gilliam et al. [27] made a fit for their data in S/cm. The relationship is shown below:

$$\kappa = A(c) + B(c^2) + C(c \cdot T) + D(c/T) + E(c^3) + F(c^2 \cdot T^2) \tag{A.1}$$

With the constants given in the table below:

Table A.1: Constants used in equation A.1

Constant	Value	Unit
A	-2.041	S cm^{-1} mol^{-1}
B	-0.0028	S cm^{-1} mol^{-2}
C	0.005332	S cm^{-1} mol^{-1} K^{-1}
D	207.2	S K cm^{-1} mol^{-1}
E	0.001043	S cm^{-1} mol^{-3}
F	-0.0000003	S cm^{-1} mol^{-2} K^{-2}

The dependency of KOH on ionic conductivity is shown in Fig. A.1

Figure A.1: Dependency of the potassium hydroxide concentration on the ionic conductivity for 25 °C on documented by Gilliam et al. [27]

Viscosity

The dependency of the viscosity on the potassium hydroxide concentration is given by Kuznetsov et al. [36]. The data is shown in figure A.2 together with a fit.

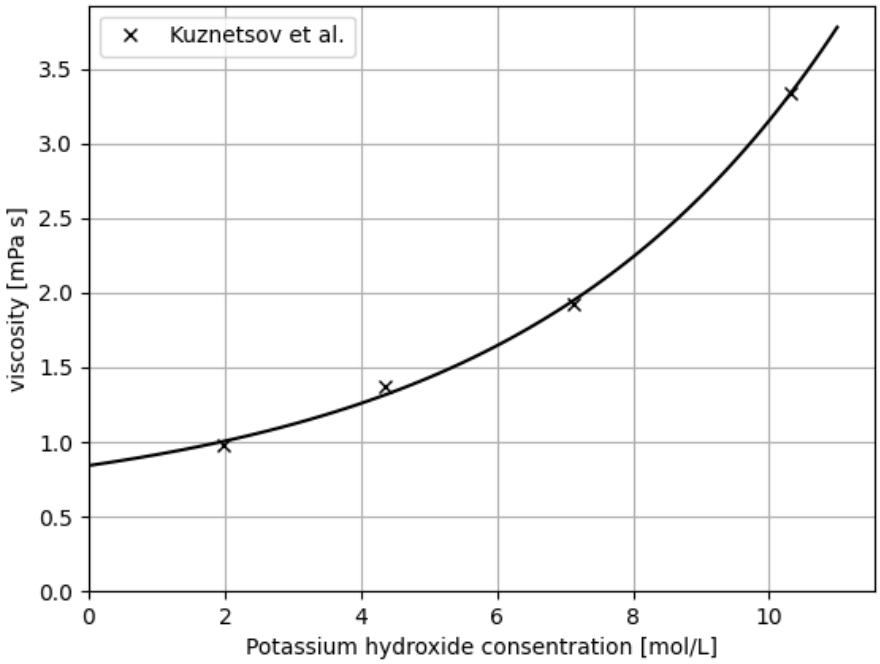

Figure A.2: Dependency of the potassium hydroxide concentration on the viscosity documented by Kuznetsov et al. [36]

The equation for the fit in units Pa s is:

$$\mu(c) = A + B\mathrm{e}^{Cc} \tag{A.2}$$

With the constants, A, B and C given in the table below:

Table A.2: Constants used in equation A.2

Constant	Value	Unit
A	$5.359 \cdot 10^{-4}$	Pa s
B	$3.064 \cdot 10^{-4}$	Pa s
C	0.2145	-

Solubility

The data for the solubility of hydrogen in water is given by Ruetschi et al. [37]. The data together with a fit are shown in figure A.3.

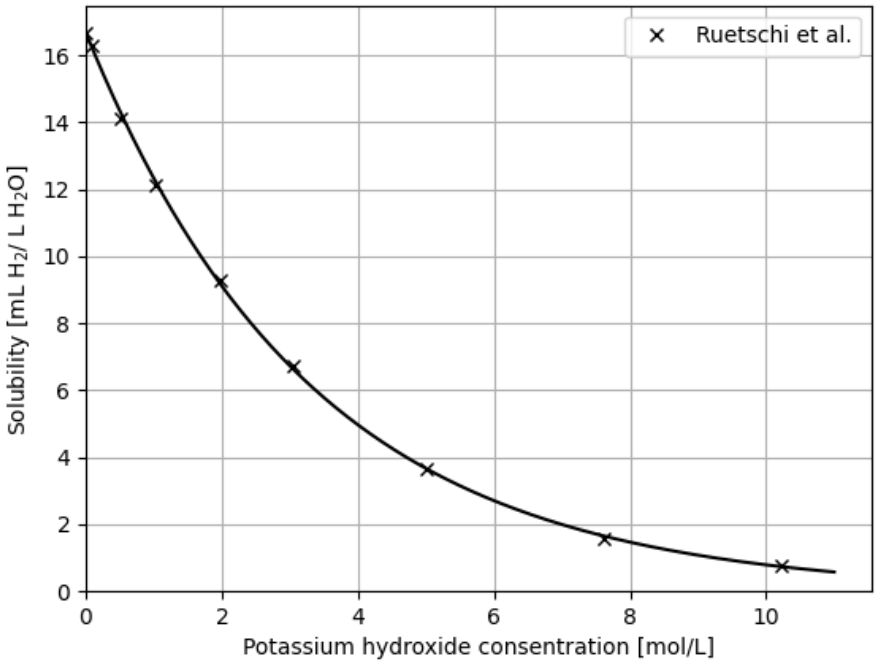

Figure A.3: Dependency of the potassium hydroxide concentration on the solubility documented Ruetschi et al. [37]

The equation for the fit in units m^3 H_2/m^3 H_2O is:

$$S_V(c) = A + B\mathrm{e}^{Cc} \tag{A.3}$$

With the constants, A, B and C given in the table below:

Table A.3: Constants used in equation A.2

Constant	Value	Unit
A	$16.715 \cdot 10^{-3}$	m^3 H_2/m^3 H_2O
B	$0.3018 \cdot 10^{-3}$	m^3 H_2/m^3 H_2O
C	-0.02786	-

Note that to get equation A.3 in units mol/m^3, the equation needs to multiplied by the specific density, ρ_{H_2}, which can be found in table 4.1

Density

The relationship between density and KOH concentration has been documented by Gilliam et al. [27]. They give the following relationship for density in units of kg/m^3:

$$\rho(c) = A \cdot c^2 + B \cdot c + C \tag{A.4}$$

With the constants, A, B and C given in the table below:

Table A.4: Constants used in equation A.4

Constant	Value	Unit
A	-0.4824	kg m^{-3} mol^{-2}
B	45.761	kg m^{-3} mol^{-1}
C	999.63	kg m^{-3}